Accuracy of the Lightning Mapping Array

Ronald J. Thomas,[1] Paul R. Krehbiel,[2] William Rison,[1] Steven J. Hunyady,[3] William P. Winn,[3] Timothy Hamlin,[2] and Jeremiah Harlin[2]

Received 16 January 2004; revised 26 April 2004; accepted 18 May 2004; published 29 July 2004.

[1] The location accuracy of the New Mexico Tech Lightning Mapping Array (LMA) has been investigated experimentally using sounding balloon measurements, airplane tracks, and observations of distant storms. We have also developed simple geometric models for estimating the location uncertainty of sources both over and outside the network. The model results are found to be a good estimator of the observed errors and also agree with covariance estimates of the location uncertainties obtained from the least squares solution technique. Sources over the network are located with an uncertainty of 6–12 m rms in the horizontal and 20–30 m rms in the vertical. This corresponds well with the uncertainties of the arrival time measurements, determined from the distribution of chi-square values to be 40–50 ns rms. Outside the network the location uncertainties increase with distance. The geometric model shows that the range and altitude errors increase as the range squared, r^2, while the azimuthal error increases linearly with r. For the 13 station, 70 km diameter network deployed during STEPS the range and height errors of distant sources were comparable to each other, while the azimuthal errors were much smaller. The difference in the range and azimuth errors causes distant storms to be elongated radially in plan views of the observations. The overall results are shown to agree well with hyperbolic formulations of time of arrival measurements [e.g., *Proctor*, 1971]. Two appendices describe (1) the basic operation of the LMA and the detailed manner in which its measurements are processed and (2) the effect of systematic errors on lightning observations. The latter provides an alternative explanation for the systematic height errors found by *Boccippio et al.* [2001] in distant storm data from the Lightning Detection and Ranging system at Kennedy Space Center. *INDEX TERMS:* 3304 Meteorology and Atmospheric Dynamics: Atmospheric electricity; 3324 Meteorology and Atmospheric Dynamics: Lightning; 3360 Meteorology and Atmospheric Dynamics: Remote sensing; 3394 Meteorology and Atmospheric Dynamics: Instruments and techniques; 6969 Radio Science: Remote sensing; *KEYWORDS:* lightning, thunderstorms, aircraft sparking, radio frequency tracking and location, data telemetry

Citation: Thomas, R. J., P. R. Krehbiel, W. Rison, S. J. Hunyady, W. P. Winn, T. Hamlin, and J. Harlin (2004), Accuracy of the Lightning Mapping Array, *J. Geophys. Res.*, *109*, D14207, doi:10.1029/2004JD004549.

1. Introduction

[2] The New Mexico Tech Lightning Mapping Array (LMA) locates the sources of impulsive radio frequency radiation produced by lightning flashes in three spatial dimensions and time [*Rison et al.*, 1999; *Krehbiel et al.*, 2000]. It does so by accurately measuring the arrival times of radiation events at a network of ground-based measurement stations spread over an area typically 60 km in diameter. The signals are received in an unused very high frequency (VHF) television band, usually channel 3 (60–66 MHz). The accuracy of the locations depends on the uncertainty of the arrival time measurements and on the number and positions of the stations used to obtain each solution. The arrival times are measured independently at each station using an accurate time base provided by a GPS receiver. In this paper we investigate the accuracy of the source locations both experimentally and theoretically and show how the experimentally observed errors are explained by the timing uncertainties and array geometry. The results can be used to design and optimize an array that meets a given set of requirements.

[3] The use of time of arrival (TOA) measurements in lightning studies was pioneered by D. E. Proctor in South Africa [e.g., *Proctor*, 1971, 1981; *Proctor et al.*, 1988]. Proctor utilized a network of five stations arrayed along two nearly perpendicular baselines to study the detailed breakdown of individual lightning discharges. The network, in the approximate form of a cross, was about 30 km in east–west (E–W) extent and 40 km in north–south (N–S) extent. The analog receiver outputs from each of the outlying stations were telemetered to the central station, where they were recorded and manually processed to

[1]Electrical Engineering Department, New Mexico Tech, Socorro, New Mexico, USA.
[2]Physics Department, New Mexico Tech, Socorro, New Mexico, USA.
[3]Langmuir Laboratory, Geophysical Research Center, New Mexico Tech, Socorro, New Mexico, USA.

0148-0227/04/2004JD004549$09.00

identify the times of common events. The arrival time differences were analyzed using hyperbolic formulations to obtain the source locations. In his initial paper on the system, *Proctor* [1971] discussed the geometric interpretation of the solutions and the effect of the network geometry on the location accuracy. The TOA measurements were made with 5 MHz bandwidth receivers at a center frequency of 300 MHz and had estimated timing errors Δt of about 70 ns rms. From this the horizontal location accuracy was estimated by Proctor to be about $c\Delta t \simeq 20$ m for sources within the boundaries of the network. Owing to the way in which the hyperbolic surfaces intersected, the vertical errors were larger and were estimated to vary from 100 m up to several hundred meters or a kilometer, depending on the altitude and horizontal location of the source relative to the measurement stations.

[4] Using Proctor's approach, *Lennon* [1975] implemented a seven station network for monitoring lightning over and around Kennedy Space Center (KSC), Florida. Called the Lightning Detection and Ranging (LDAR) system, the network consisted of an approximately circular array of six measurement stations about 16 km in diameter concentric with a central seventh station. Conceptually and for processing purposes, the network was considered to consist of two Y-shaped arrays, one upright and the other upside down, each consisting of three outlying stations and the central station. Logarithmically detected RF signals from the outlying stations were telemetered in analog form to the central station, as in Proctor's system, but were then digitized with 50 ns time resolution and were automatically processed to obtain the lightning sources in real time. The system typically located several tens of events per lightning flash [e.g., *Krehbiel*, 1981]. In addition to being important for operations at Kennedy Space Center (KSC) and the Cape Canaveral Air Force Station, the LDAR system provided valuable information on the storms during the Thunderstorm Research International Program (TRIP 76–78) [e.g., *Lhermitte and Krehbiel*, 1979].

[5] The accuracy of the LDAR system was studied by *Poehler* [1977], who estimated the location uncertainties over the network from geometric dilution of precision formulations for an ideal Y-shaped array and performed Monte Carlo simulations of the location accuracy outside the network. Assuming 20 ns rms timing errors, the results indicated 7–11 m rms uncertainties in plan locations over the network and an order of magnitude larger (72–100 m rms) errors in the vertical for sources at 8 km altitude. Outside the network the location uncertainties were found to be much greater in range than in azimuth; the location uncertainties were considered to be acceptable to 32 km range (500 m rms error in range and 250 m error in altitude). Poehler confirmed the error results by analyzing the scatter in an airplane track that (for then unknown reasons) was detected by the LDAR system and by analyzing system calibration data provided by spark generators located on the top of two buildings at KSC.

[6] An improved, second-generation version of the LDAR system was developed by Lennon and coworkers at Kennedy Space Center in the early 1990s [*Maier et al.*, 1995]. Observations from the new LDAR system were studied statistically by *Boccippio et al.* [2001] for a 19 month period during 1997–1998, including the two summer convective seasons. The distribution of located lightning sources was determined as a function of height and range out to 300 km distance from the network. The areal density of sources was found to decrease exponentially with range, inconsistent with and more rapidly than would be predicted by signal detectability (i.e., signal-to-noise ratio) considerations. Also, the height of the maximum lightning activity was found to increase systematically with range, from a physically correct value of 9 km altitude over and close to the network to a physically incorrect value of about 20 km altitude at 300 km range. The authors summarized results from other TOA systems, including early results from the Lightning Mapping Array, which indicated that the range errors outside the network increased as the range squared (r^2). From a Monte Carlo analysis of their analytic formulations, Boccippio et al. inferred that the systematic height increase with distance resulted from the system having unexpectedly large range errors at large distances. The sources at large range were thought to be dominated by overranged sources in storms at intermediate ranges, which would appear to be at higher altitudes.

[7] The problem of retrieving source locations from TOA measurements has also been studied by *Koshak and Solakiewicz* [1996] (hereinafter referred to as KS96) and by *Koshak et al.* [2004]. KS96 developed an alternative formulation to the nonlinear hyperbolic equations used by Proctor and Lennon for retrieving the source locations. Their formulation recast the TOA equations in a linear form and enabled solutions and error analyses to be obtained analytically. *Koshak et al.* [2004] applied the results of KS96 to develop a more complete source retrieval algorithm and used it in a theoretical study of the errors in an LMA being operated in north Alabama [e.g., *Goodman*, 2003]. The retrieval algorithm is basically the same as that developed to process LMA observations (Appendix A).

[8] In the present study we examine the accuracy of the Lightning Mapping Array both experimentally and theoretically. We separate the problem into two regimes by investigating the location uncertainties first over or near the array and then outside the array. In each regime we develop simple geometric models which describe the basic way in which the measurements determine the source locations and give the functional behavior of the location accuracies. The model results are compared with experimentally observed errors from a sounding balloon and from aircraft tracks and with the results of linearized covariance analyses from the solution technique. The results confirm and extend many of the findings of the previous studies, correct some other findings, and elaborate on several practical aspects of the observations. The models provide simple analytic formulations for the errors that are in good agreement with the experimental results and show, for example, why the range errors increase as r^2. The effect of systematic errors is discussed in Appendix B, which includes an alternative explanation for the systematic height increase found by *Boccippio et al.* [2001] in the LDAR observations.

[9] The data of this study were obtained while the LMA was being operated in the Severe Thunderstorm Electrification and Precipitation Study (STEPS 2000) in northwestern Kansas and eastern Colorado [*Lang et al.*, 2004; W. D. Rust et al., Inverted-polarity electrical structures in thunder-

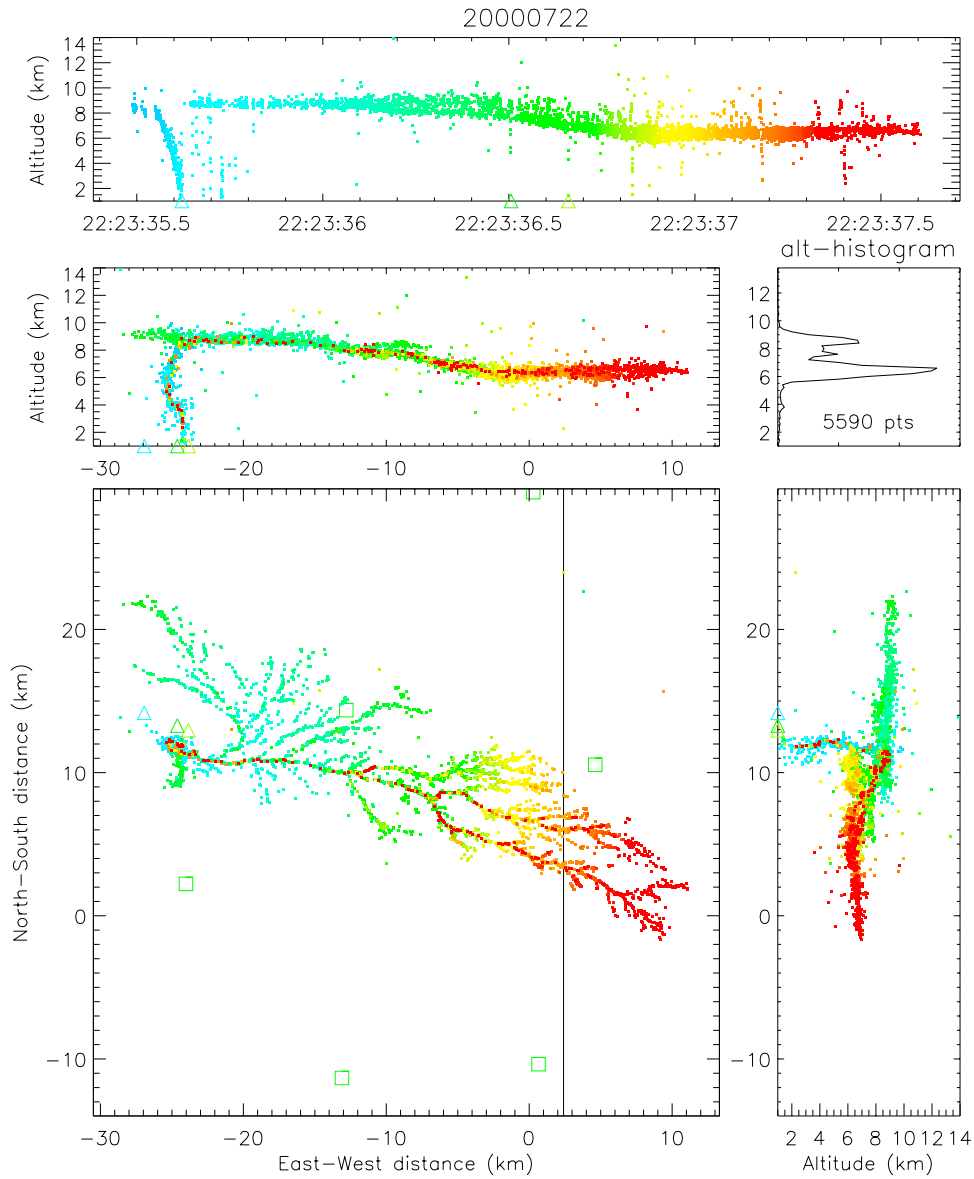

Figure 1. Radiation sources for a negative polarity cloud-to-ground discharge that occurred over the northern end of the STEPS network at 2223:35–37 UTC on 22 July 2000. The colors indicate time progression, and the different panels show the evolution of the flash in (top) height-time, (bottom left) plan view, and in (middle left) east–west (E–W) and (bottom right) north–south (N–S) vertical projections. Also shown is a histogram of the source heights. The triangles indicate negative ground strike times and locations from the National Lightning Detection Network (NLDN). The squares in the plan view indicate the location of measurement stations, and the vertical line denotes the Colorado-Kansas state border.

storms in the Severe Thunderstorm Electrification and Precipitation Study (STEPS), submitted to *Atmospheric Research*, 2003]. A brief description of the mapping system and of the processing approach used to obtain the source locations is given in Appendix A.

2. Lightning Example

[10] Figure 1 shows an example of a lightning discharge observed by the LMA during STEPS that illustrates the spatial resolution that the system is able to obtain. The flash was a negative polarity cloud-to-ground (CG) discharge that occurred over the northern part of the network and was accurately located by the measurements. The discharge propagated over a large horizontal distance (40 km) through its parent storm; in the process the breakdown channels developed a fine dendritic structure that was well resolved by the mapping system. More than 5000 sources were located during the 2 s duration of the flash.

[11] Data from the National Lightning Detection Network (NLDN) [*Cummins et al.*, 1998] show that the flash was a multiple-stroke CG discharge that lowered negative charge to ground. The top panel of the figure shows the altitude of the sources versus time and indicates that the initial stepped

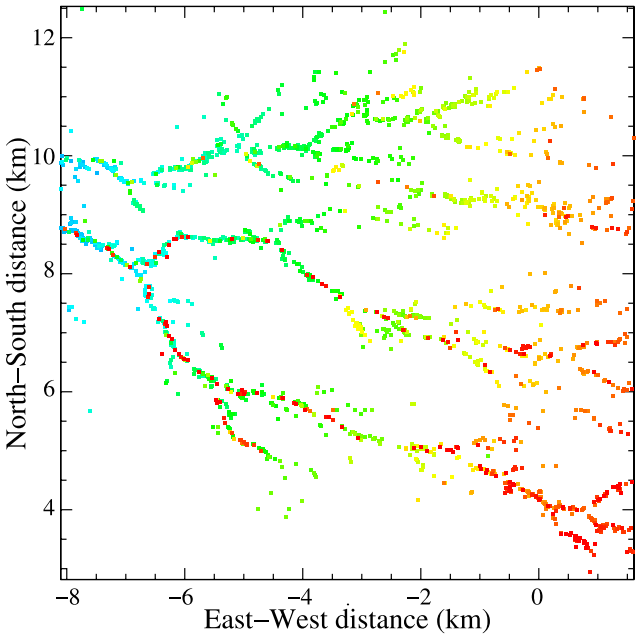

Figure 2. Expanded plan view of the dendritic structure of the flash of Figure 1, showing the level of detail in the observations and the accuracy with which several breakdown events near the end of the flash retrace the earlier channels (red sources).

leader initiated between 8 and 9 km altitude, after about 50 ms of preliminary breakdown, and required about 60 ms to reach ground. (All altitudes in this study are GPS altitudes, which are within about 10 m of mean sea level.) The NLDN observed the initial stroke and two subsequent strokes at the times and locations indicated by the triangles in the figure. Similar but less extensive horizontal flashes were studied by *Krehbiel et al.* [1979], who showed that sources of charge for successive strokes developed horizontally away from the flash initiation region.

[12] The colors of the sources indicate time progression; when viewed in time animation, the flash steadily developed outward along the various branches, with multiple branches extending simultaneously in time. The TOA technique and the processing are readily able to sort out the resulting "back and forth" activity of the different branches. The subsequent strokes were initiated by fast dart leaders, for which only a few sources were located by the mapping system. Such leaders typically last only a few hundred microseconds and therefore are not well sampled by the 80 or 100 μs measurement windows with which the LMA usually operates. The lack of a second stepped leader in the LMA data indicates that all strokes went down a single channel to ground. A final breakdown event at 37.4 s near the end of the flash (shown in red) traversed the complete horizontal extent of the discharge and progressed downward toward ground. It would appear to have initiated another stroke but most likely was an attempted leader of the type reported by *Shao et al.* [1995].

[13] Figure 2 shows an expanded view of a 10-km-wide section of the channels to indicate their detailed structure. The dots used in Figure 2 have a size of about 100 m, which, as will be seen, is comparable to or larger than the plan location accuracy with which the system is able to locate impulsive events. While many of the individual channels are well resolved, the lateral spread of the sources along the channels is comparable to or slightly larger than the dot sizes. This is indicative of unresolved additional structure in the breakdown channels and/or of location uncertainties introduced by the sources not being completely impulsive. The late-stage breakdown (red sources) retraced the earlier channels with good accuracy.

[14] In addition to fine-scale "noisiness" in the channel structure, a relatively small number of sources have kilometer or larger errors. These are seen in the vertical projection panels of Figure 1 as outlying points both above and below the horizontal channels and alongside the channel to ground. The outlying points can be identified as being incorrect because of the limited vertical extent of the in-cloud breakdown and the relatively localized and unbranched initial leader channel. As discussed in section 3, the outlying points result from the occasional incorporation of random local noise events at a station into the set of data values used to obtain the solutions. For analyses of individual flashes, outlying points can be removed by manually editing the observations and/or by tightening goodness of fit restrictions. Sections 3–6 present detailed analyses of the accuracy of the mapping system for sources over and outside the network.

3. Location Accuracy Over the Network

[15] We first investigate the location errors for sources over or near the network of measurement stations. The errors were determined experimentally by using the mapping array to locate a sounding balloon that carried a GPS receiver and a VHF transmitter. The results are found to be in good agreement with error estimates from a simple geometric model and with linearized estimates of the location uncertainties obtained from the least squares solution technique.

[16] Several experiments were conducted during STEPS in which the LMA was used to track sounding balloons carrying a pulsed VHF transmitter. The transmitter broadcast short-duration (125 ns) pulses of 63 MHz radiation, which were located by the LMA as the balloon ascended. One sounding balloon carried a handheld GPS receiver (Magellan GPS 310) that determined the balloon location every second. A serial bit stream containing the GPS location data was transmitted to the ground by modulating the time between transmitted pulses. The pulse transmission rate averaged about 140 s^{-1}, and more than 500,000 pulses were located during the ~1 hour flight. Details of the modulation and decoding technique are presented in Appendix D.

[17] Figure 3 shows the flight path of the GPS sounding balloon as determined by the mapping system. Figure 3 also shows the network of measurement stations used during STEPS. Thirteen stations were deployed over an area about 80 km in E–W extent and 60 km in N–S extent. The balloon was launched near the center of the network and ascended to about 24 km altitude. In the process it drifted eastward to slightly beyond the network's northeastern edge. The rubber balloon burst at 24 km altitude, after which the instrument rapidly descended to about 19 km

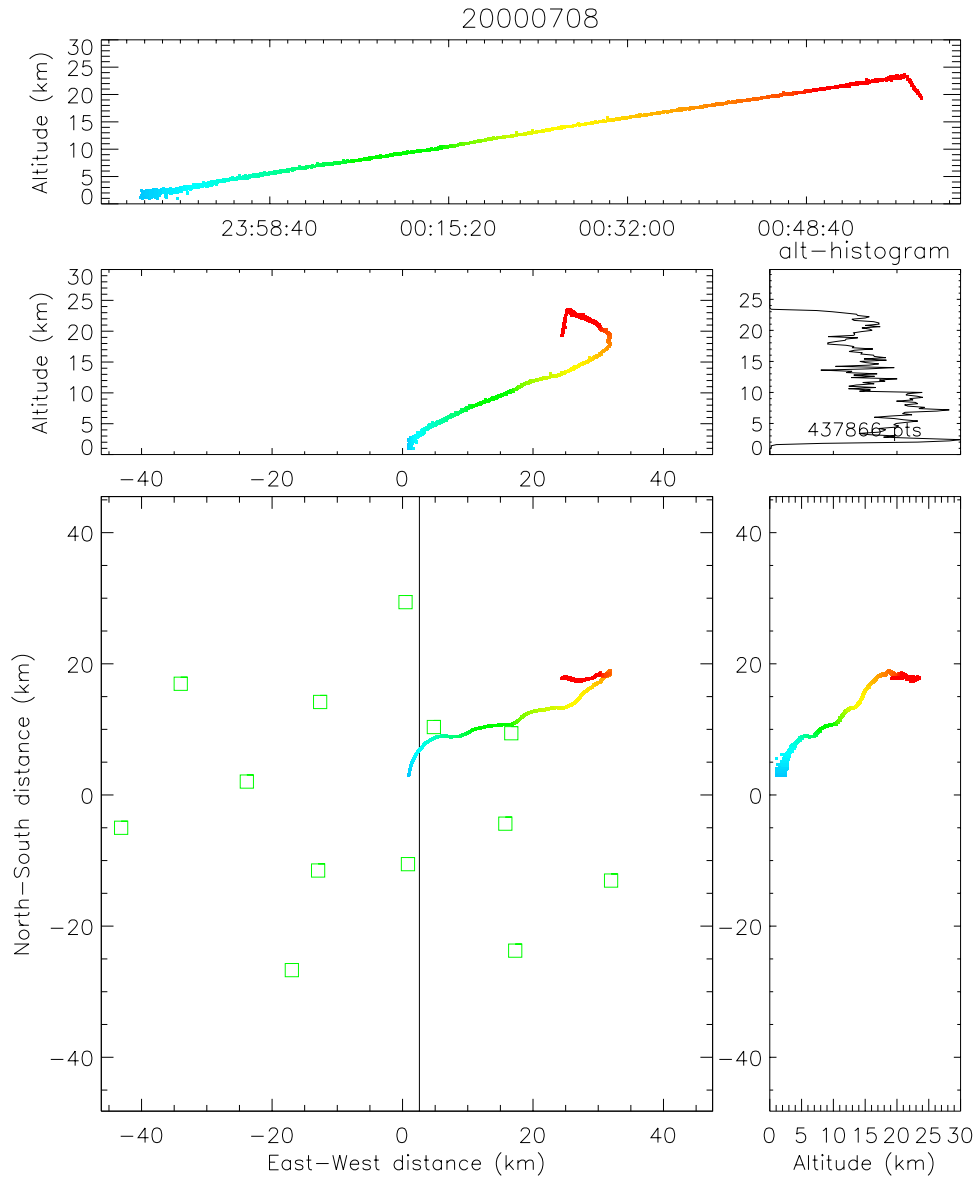

Figure 3. Trajectory of the balloon flight as located by the Lightning Mapping Array (LMA) relative to the network of 13 mapping stations (green squares). The (lower left) plan view and (middle right) altitude projections show that the balloon drifted eastward as it ascended, crossing from Colorado into Kansas shortly after launch. The balloon rose for about an hour, encountering easterly winds above 19 km altitude and (top) bursting at 23.5 km. Only events located by at least eight stations are displayed. The coordinate origin was near the center of the network at the location of a lightning interferometer and electric field change sensor.

altitude before the transmitter ceased functioning. The flight took place between 1800 and 1900 LT on 9 July in clear-weather conditions with no nearby storms.

[18] Figure 4 shows successively expanded views of the LMA balloon track (red dots) and the onboard GPS locations (central black line). The data are shown in E–W vertical projection. The expanded view in the lower right panel shows that most of the LMA source locations were within ±50 m of the GPS track. The location differences were determined by fitting the GPS track with a sequence of third-order polynomials over consecutive 10 s time intervals. The GPS locations were then interpolated to the time of each transmitted pulse, and the mean and standard deviation of the difference values were evaluated over each kilometer interval along the track. The mean difference in each interval was typically about 15 m and could have resulted from uncertainty in the onboard GPS location itself. Histograms of the difference values show that >99% of the locations were normally distributed about the mean, with standard deviations between 10 and 30 m (an example is shown in Figure 8). About 1% of the located sources exhibited larger errors, up to several kilometers, and correspond to the outlying points in Figure 4. The periodic fluctuations of the source heights seen in the lower right panel are due to small systematic timing errors, discussed in Appendix B. As required by

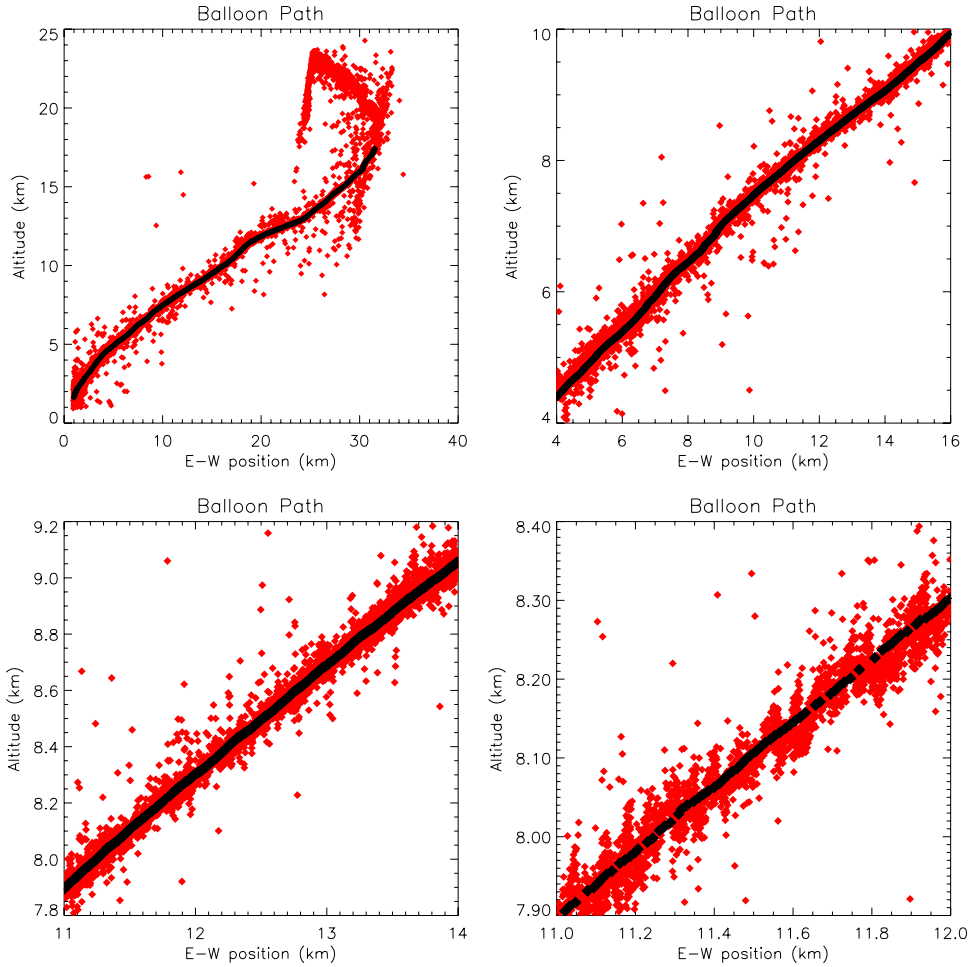

Figure 4. E–W vertical projection of the balloon trajectory as determined by the onboard GPS receiver (black line) and from LMA locations of the RF transmitter pulses (red dots). (top left) Entire trajectory; remaining panels show increasingly expanded portions of the trajectory. All source locations (from six or more stations) are shown. The "noisiness" of the LMA-determined trajectory in the less expanded views is due to <1% of the sources incorporating a random noise event at one of the stations (see text) and is exaggerated by the relatively large dot size, which makes each point visible. Most points lie within a few tens of meters or less of the GPS-determined track.

federal regulations, the GPS receiver did not provide location values above ≃17.5 km.

[19] Figure 5 shows the standard deviations of the location differences in each Cartesian direction. Up to about 10 km altitude, the location uncertainty was between 6 and 12 m rms in the E–W and N–S directions. The altitude uncertainty was typically 2–3 times greater, between about 20 and 30 m rms. The increase seen in the E–W and N–S

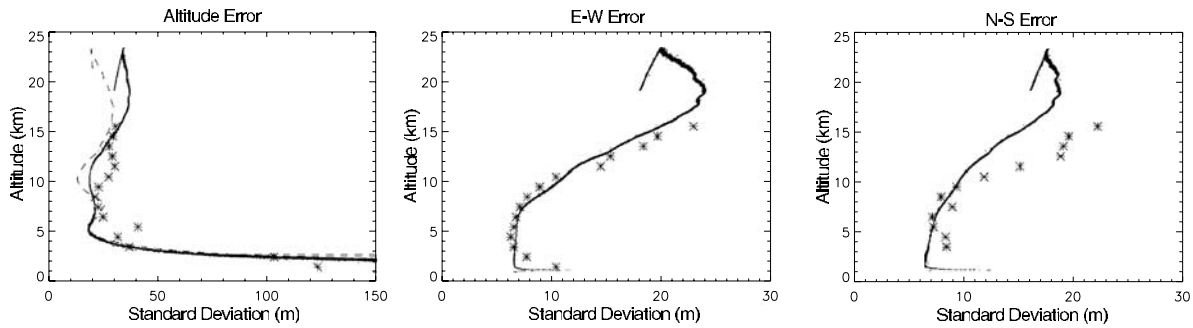

Figure 5. Standard deviation of the difference in the LMA and GPS balloon locations versus altitude (asterisks) in the three Cartesian directions. The solid line in each panel shows the average rms location uncertainty from the covariance matrix of the solutions; the dashed line in the altitude error panel shows the error estimated from the simple geometric model of Figure 6b.

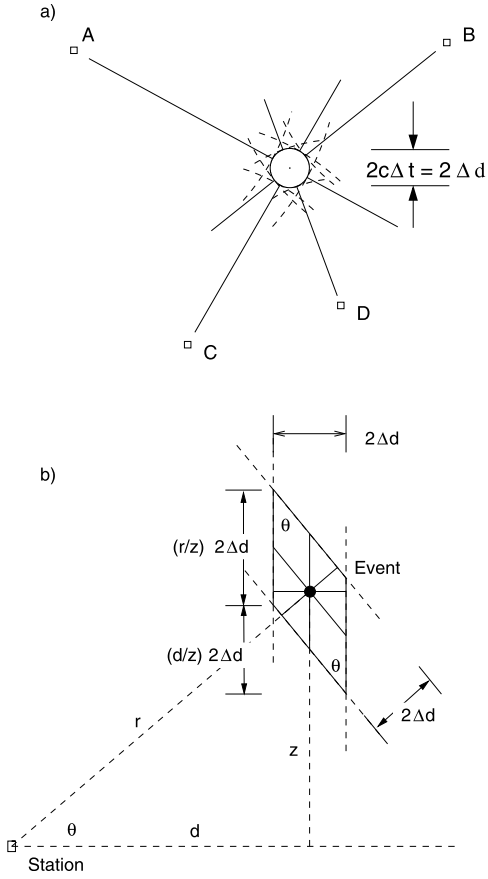

Figure 6. Simple geometric models for the location uncertainty of sources over the network. (a) Plan view indicating how distant stations constrain the plan location to an approximate circle of radius $\Delta d = c\Delta t$. (b) Vertical cross section indicating how a close station enables the altitude of the source to be determined.

errors above 7 km altitude occurred as the balloon drifted toward and outside the northeastern boundary of the network. Below about 3 km altitude (2 km above ground level) the altitude uncertainty rapidly increased to more than 100 m rms.

[20] The expected values of the location errors can be estimated from simple geometric considerations, as indicated in Figure 6. The horizontal uncertainty is determined primarily by distant stations (Figure 6a). The plan location is constrained by the measurements at each station to be within a radial distance $\Delta d \simeq \pm c\,\Delta t$ from its actual location, where Δt is the rms timing uncertainty. Measurements in different directions from the source therefore restrict the plan location to an approximate circle of diameter $2\Delta d = 2c\Delta t$. For an assumed error $\Delta t \simeq 40$ ns, $\Delta d \simeq 12$ m. This simple model, also used by *Proctor* [1971] and *Poehler* [1977], slightly overestimates the measured errors, which are between 6 and 12 m rms (Figure 5).

[21] The above model represents the solution as the intersection of circles concentric with each station and implicitly assumes that the source time is known. The model can be refined by noting that although the source time is not known, when the source is situated along the baseline between two measurement stations, the location accuracy corresponds to half the uncertainty in the difference in arrival times. Because the errors are uncorrelated at the two stations, the rms error in the arrival time difference is $\sqrt{2}\,\Delta t$. Thus $\Delta d = (1/2)\,c\sqrt{2}\,\Delta t = (1/\sqrt{2})\,c\,\Delta t = 8.5$ m. Since sources over the central part of the network are effectively surrounded, the refined result is the appropriate one and is in good agreement with the observed errors. To the extent that multiple sets of stations are involved in the horizontal locations, the error can be somewhat smaller, as observed.

[22] The altitude of the source is determined primarily by the arrival time at the closest station (Figure 6b). The altitude has the smallest uncertainty when the source is directly above a station and increases for sources that are displaced horizontally away from the station. The uncertainty in the radial distance r from the close station is the same as the horizontal uncertainty for distant stations, namely $\pm c\Delta t$. From the geometry of the resulting parallelogram the rms error in the height z is given by

$$\Delta z \simeq c\,\Delta t\left(\frac{d+r}{z}\right), \tag{1}$$

where d is the horizontal distance of the source from the close station. When the source is directly above the station, $d = 0$ and $r = z$, giving that $\Delta z \simeq c\Delta t$, as expected. For the general case in which $d \neq 0$ the vertical uncertainty is greater than the horizontal by a factor of $\Delta z/\Delta d \simeq (d + r)/z > 1$. This is also seen in the experimental results. For source heights equal to half the distance between stations (in our case, $z = 5$–10 km above ground level), $d_{\max} \simeq z$ and $r \simeq \sqrt{2}\,z$, so the ratio of the vertical to horizontal errors is $\Delta z/\Delta d \simeq 1 + \sqrt{2} = 2.4$. This is in good agreement with the observations that the vertical errors were 2–3 times the horizontal errors. For z small compared to d and r the vertical error becomes increasingly large.

[23] The estimate of the height uncertainty from equation (1) is shown by the dashed curve in the left panel of Figure 5, assuming $\Delta t = 40$ ns. The curve was determined using the actual distance of the balloon from the nearest station. The separate minima at 5 km and 10 km altitude correspond to the balloon passing nearly over two stations as it ascended. The minima correspond to relative maxima in the measured errors, however, because of signal dropouts when the balloon was above or nearly above a station. (The dropouts are more clearly evident in the data of Figure 7, discussed below, and are due to the vertical dipolar antennas of both the transmitting and receiving antennas pointing toward each other, i.e., being close to or in the nulls of their antenna patterns.) The model results are otherwise in good agreement with the measured errors.

[24] The geometric interpretations of the simple error models are compared with those obtained from the hyperbolic approach used by *Proctor* [1971] in section 6 of this paper.

[25] The location uncertainties can also be determined from an error analysis of the equations used to obtain the solutions. As discussed in Appendix A, the source locations are obtained using a standard iterative least squares procedure (the Levenburg-Marquardt algorithm) to solve the nonlinear TOA equations [e.g., *Bevington*, 1969]. The algorithm linearizes the equations around successive trial solutions, and the linearization for the final solution gives a

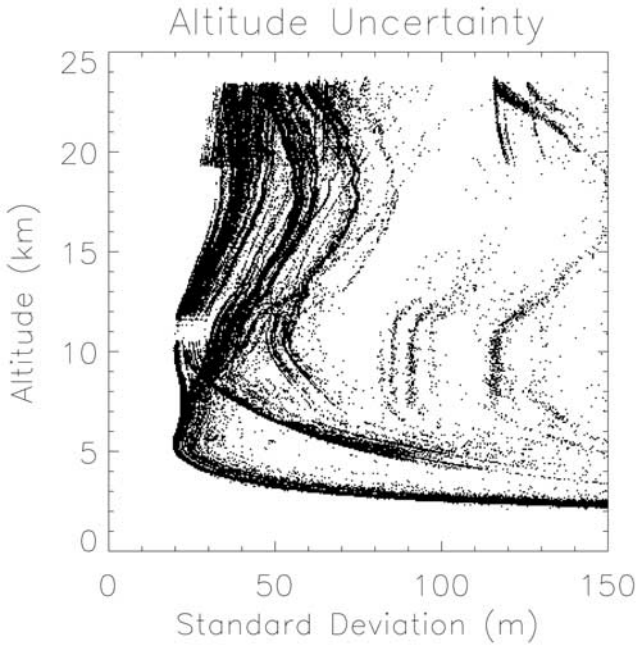

Figure 7. Covariance estimates of the altitude uncertainty for each transmitted pulse during the balloon flight. The results group into curves associated with different combinations of stations being used to locate the pulses. Sets of curves having larger uncertainty correspond to less favorable sets of stations participating in the solution. The blanked out sources around 11 km altitude in the leftmost set of curves resulted from signal dropouts as the balloon passed directly above the northeast station (Figure 3).

covariance matrix describing the location uncertainties. The linearized error estimates are a good approximation to the actual uncertainties if the measurement errors are sufficiently small. The validity of the covariance error estimates was checked using a Monte Carlo simulation, which showed that the uncertainties are well approximated by the linearized equations and that normally distributed timing uncertainties give normally distributed position uncertainties. (*Koshak et al.* [2004] made a detailed comparison of the linearized covariance error estimates with Monte Carlo simulations; they found that both approaches gave similar horizontal errors but that the linearization approximation gave slightly larger vertical errors than the Monte Carlo simulation for sources outside the network.)

[26] The covariance-estimated errors for the balloon measurements are shown by the solid curve in each of the panels of Figure 5. The rms timing uncertainty was again assumed to be $\Delta t = 40$ ns, and the closest nine stations were used for determining the covariances. The results are in good agreement with the observations. The increase with altitude of the measured E–W and N–S errors is due to the balloon drifting outside the northeast periphery of the network. The increase is well matched by the covariance results in the E–W direction but is underestimated in the N–S direction. The cause of the latter difference is not understood. The altitude uncertainties from the covariance analysis agree well both with the measured errors and with the estimates from the simple geometric model.

[27] Figure 7 shows a scatter diagram of the covariance-estimated height uncertainty for each RF pulse during the balloon flight. In this case the covariance values correspond to the actual stations used to locate each event. The different families of curves correspond to different sets of stations being used to locate the events, with the larger uncertainties corresponding to less favorable combinations or numbers of stations. The missing solutions near 11 km altitude in the leftmost set of curves occurred while the balloon was above the northeast station and resulted from signal dropouts at that station, discussed above. The leftmost family of covariance values (constituting most of the points in the plot) are in good agreement with the measured values of Figure 5 (left).

[28] Figure 8 shows a histogram of the vertical location errors for sources between 10 and 11 km altitude. The central part of the distribution is well fit by a normal distribution whose mean is 10 m and standard deviation is 23 m. This corresponds to >99% of the data points and includes most of the points in this altitude range from Figure 7. The tails of the distribution are not well fitted by the normal distribution and reflect a relatively small number of solutions having significantly larger errors, up to 1 km or larger. These "bad" points most likely result from the inclusion of an incorrect TOA value (or values) in the data used to obtain the solutions.

[29] Incorrect TOA values are produced when the signal of interest is overridden by randomly timed, larger-amplitude signals from local noise sources at one or more stations. Local noise signals are produced by corona from nearby transformers and power lines (or in storm conditions, from elevated objects exposed to strong electric fields) and, at lower VHF frequencies, are always present in the data from each station. A variety of other man-made signals can also contribute to local site noise. As discussed in Appendix A, only the strongest event in successive 100 or 80 μs time windows has its time recorded; it is not

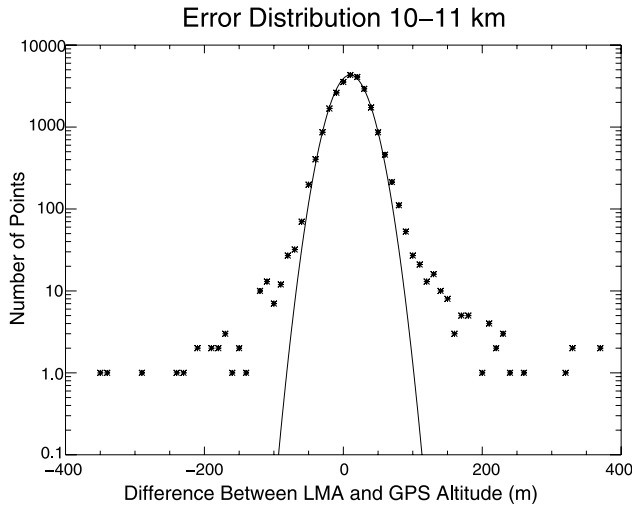

Figure 8. Histogram of the difference between the LMA and GPS location values between 10 and 11 km altitude. The solid line shows a normal distribution fitted to the data; the distribution has a mean value of 10 m and a standard deviation of 23 m and fits over 99% of the data points.

uncommon for a local noise signal to be stronger than and preempt distant lightning signals in a given time window.

[30] Almost all local noise events are rejected by the data processing because only events with correlated sets of arrival times at the different stations correspond to a common source. To aid in the rejection, we require that a minimum of six stations participate in the solution for the four unknowns (x, y, z, and t) of each event, providing at least two redundant measurements (degrees of freedom) as a check on the validity of the solution. However, local noise events are unavoidably incorporated into some solutions. This is also evidenced by the outlying points along the balloon trajectory in the different panels of Figure 4. The outlying points can be reduced by increasing the minimum number of stations required to participate in the solutions. Figure 3 shows only the sources located by eight stations, which eliminated all outlying points.

[31] To test that the outlying locations were caused by the incorporation of noise signals, we performed a six station Monte Carlo simulation in which normally distributed errors with a standard deviation of 70 ns were added to the arrival times at the different stations of a simulated event. For one station chosen at random, an additional error uniformly distributed over ± 7 μs was added. (The value of 7 μs corresponded to the time window of acceptance over which the data from a given station could be used in a solution.) Solutions were occasionally obtained that had goodness of fit values low enough to be considered a valid solution (and therefore would have been included in the data points of Figures 7 and 8) but whose location was substantially displaced from the correct one and therefore would have been in the "bad" point tail of the distribution in Figure 8. For simulated solutions having reasonable goodness of fit values it was not possible to identify which station contributed the bad data point from the residues of the least squares fit. Similarly, we have not been able to identify bad data points in nonsimulated solutions having reasonable goodness of fit values.

3.1. Chi-Square Distributions

[32] Excluding bad data points, the above mentioned results indicate that the effective timing errors of the LMA system were about 40 ns rms for the balloon sounding data. The timing errors can be more precisely determined by examining the goodness of fit values of the solutions. (The goodness of fit is given by the reduced chi-square value χ^2_ν of the solution, discussed in Appendix A.) In particular, one can compare the distribution of reduced chi-square values for the solutions with the theoretical distributions. The theoretical distributions are given by *Bevington* [1969] and assume the measurement errors are Gaussian distributed.

[33] Figure 9 shows the observed and theoretical distributions of the reduced chi-square values. Separate comparisons are made for different values of the number of degrees of freedom, i.e., for solutions obtained from different numbers of stations. The solutions were obtained assuming a nominal 70 ns rms timing error at each station, but the chi-square values are readily scaled to an rms error of any Δt by multiplying by a factor $(70 \text{ ns}/\Delta t)^2$. The reduced chi-square values shown in Figure 9 have been adjusted to correspond to an rms error $\Delta t = 43$ ns and are in good agreement with the theoretical distributions. This refines the value of the timing uncertainty and demonstrates that the timing errors are Gaussian distributed.

[34] The timing uncertainty is slightly larger when fewer stations participated in the solutions than when more stations participated. For 10 station solutions (the most numerous) the best fit corresponds to $\Delta t = 43$ ns, while for six station solutions the best fit corresponds to $\Delta t = 48$ ns. Assuming that the six station solutions corresponded to weaker signals on average, the increase in the timing errors is likely caused by the receiver signal-to-noise ratio being smaller for weaker signals.

[35] Figure 10 shows the same type of analysis for actual lightning data. The timing error is slightly larger for the lightning signals and was about 50 ns rms. Again, the rms error increases as the number of stations participating in the solutions decreased, from about 46 ns for 10 station solutions to 53 ns for six station solutions. In contrast with the balloon data, however, the number of located sources does not go to zero with increasing chi-square but has a "tail" of approximately constant number density for adjusted chi-square values greater than about 2. The tail indicates the presence of non-Gaussian errors, for example, from the inclusion of local noise events as discussed in section 3 or from some lightning signals being non-impulsive, having their peak amplitudes at slightly different times at the different stations.

[36] Whereas Figure 9 shows that the balloon transmitter pulses were most often located by 10 stations, the lightning events were most often located by only six or seven stations. Of 1.3 million events located during the 10 min time interval of the lightning data, 60% were located by only six stations, 81% were located by six or seven stations, and 92% were located by eight stations or less. This behavior is typical and reflects the increase in the number of lightning sources with decreasing power. From the study by *Thomas et al.* [2001], the number of located sources typically varies as $1/P$, where P is the estimated source power. As the source power approaches the network's minimum detectable level, located events will tend to be detected by the minimum number of stations.

3.2. Summary

[37] The effective timing errors of the LMA system are found to be about 43 ns rms for the deterministic transmitter pulses (i.e., pulses having a well-defined shape) and about 50 ns rms for lightning signals. The 50 ns uncertainty for lightning is found to vary somewhat with the number of stations participating in the solutions and also for different storms or time intervals but is representative of the STEPS data. For sources between about 6 and 12 km altitude over the central part of the network, the location accuracies are 6–12 m rms in horizontal position and 20–30 m rms in the vertical. The location accuracies are degraded somewhat for events over or outside the periphery of the network.

4. Location Accuracy Outside the Network

[38] Outside the mapping network the location uncertainties increase with distance from the array. In this

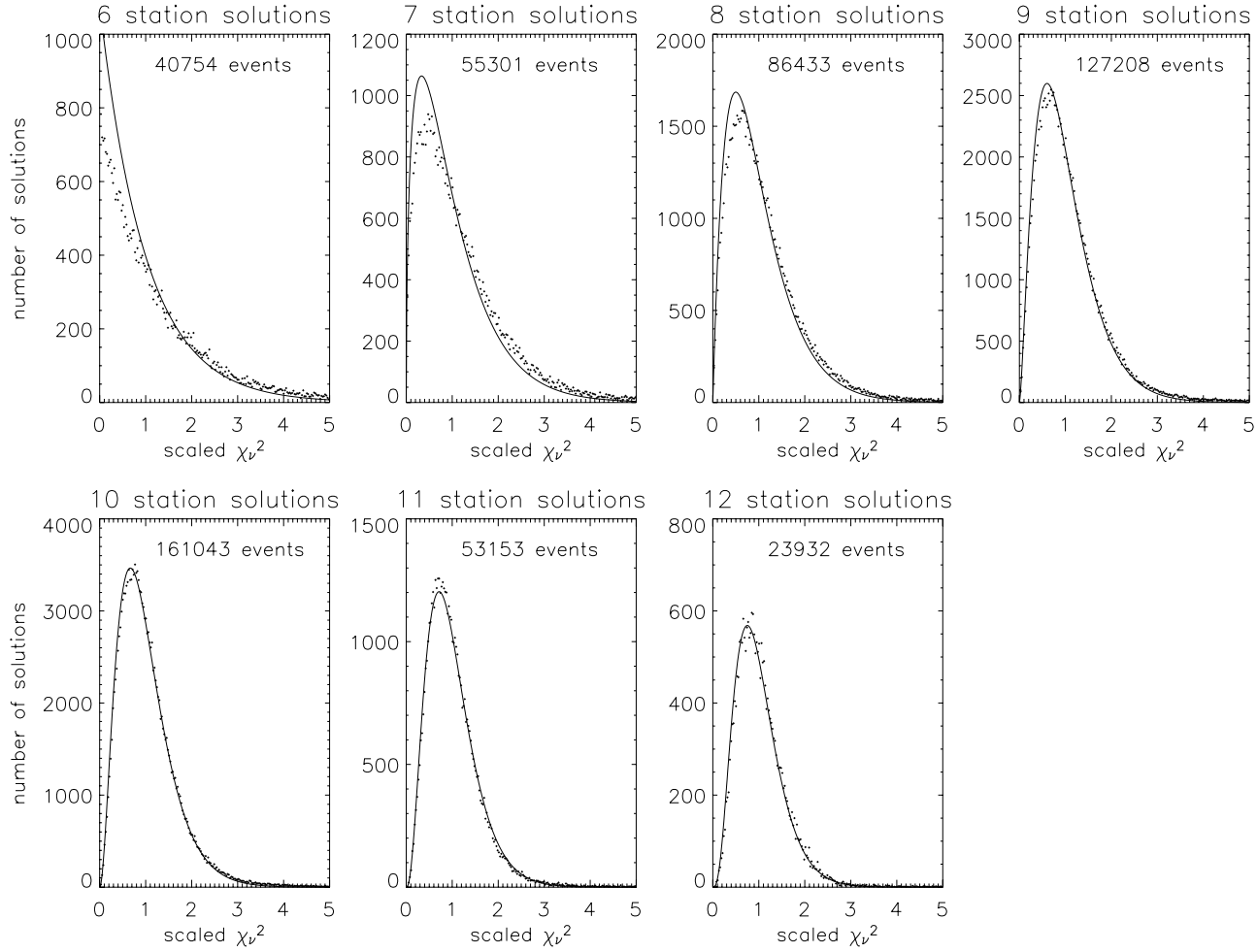

Figure 9. Distribution of reduced chi-square (χ^2_ν) values during the balloon sounding for different number of degrees of freedom $\nu = N - 4$. The χ^2_ν values have been adjusted to correspond to an rms timing error $\Delta t_{\rm rms} = 43$ ns, which gives good agreement with the theoretical distribution (solid lines). The effective timing uncertainty varied slightly with the number of stations N that participated in the solutions, ranging from 43 ns for ten station solutions (the most numerous) to 48 ns for six station solutions.

section we present a simple geometric model that shows the basic way a TOA network locates distant events. The model provides analytic formulations for the source locations that enable the increase of the location uncertainties with distance to be expressed analytically as well. The model-predicted errors are verified by comparing them with covariance results for the location uncertainties and, in section 5.1, with observations of aircraft tracks and distant storms.

[39] Consider a five station network in the form of a cross- or plus-shaped array, as shown in Figure 11a. The source to be located is assumed to be situated a relatively large distance to the right (east) of the network, approximately off the end of the E–W (x) baseline. Conceptually, the network is considered to consist of stations S2 and S4 along the x baseline, called the longitudinal baseline, and stations S0, S1, and S3 along the N–S or y baseline, called the transverse baseline. For simplicity the network is assumed to have the same extent D in both the E–W and N–S directions. For an actual network, D would correspond to the network diameter.

[40] The network locates distant events by determining the range, azimuth, and elevation angles of a source from the center of the array. In other words, the measurements determine the spherical coordinates (r, θ, ϕ) of the source relative to the network. Referring to Figure 11, the radius r of a source (also referred to as the slant range) is determined from the curvature of the wavefront, primarily as it arrives at the transverse stations (S0, S1, S3). The azimuth angle ϕ is determined primarily from the difference in the arrival times at the two ends of the transverse baseline (S1 and S3). The elevation angle θ is determined primarily by the arrival times at the longitudinal stations (S2 and S4). To keep the formulations simple, no attempt is made to incorporate redundant measurements into the model; the redundancies slightly reduce the timing uncertainties but do not otherwise affect the basic results.

[41] The conceptual array is essentially the same as the five station network used by *Proctor* [1971]. Networks with greater redundancy consist of 7 to 10 or more stations deployed over an approximately circular area so that there

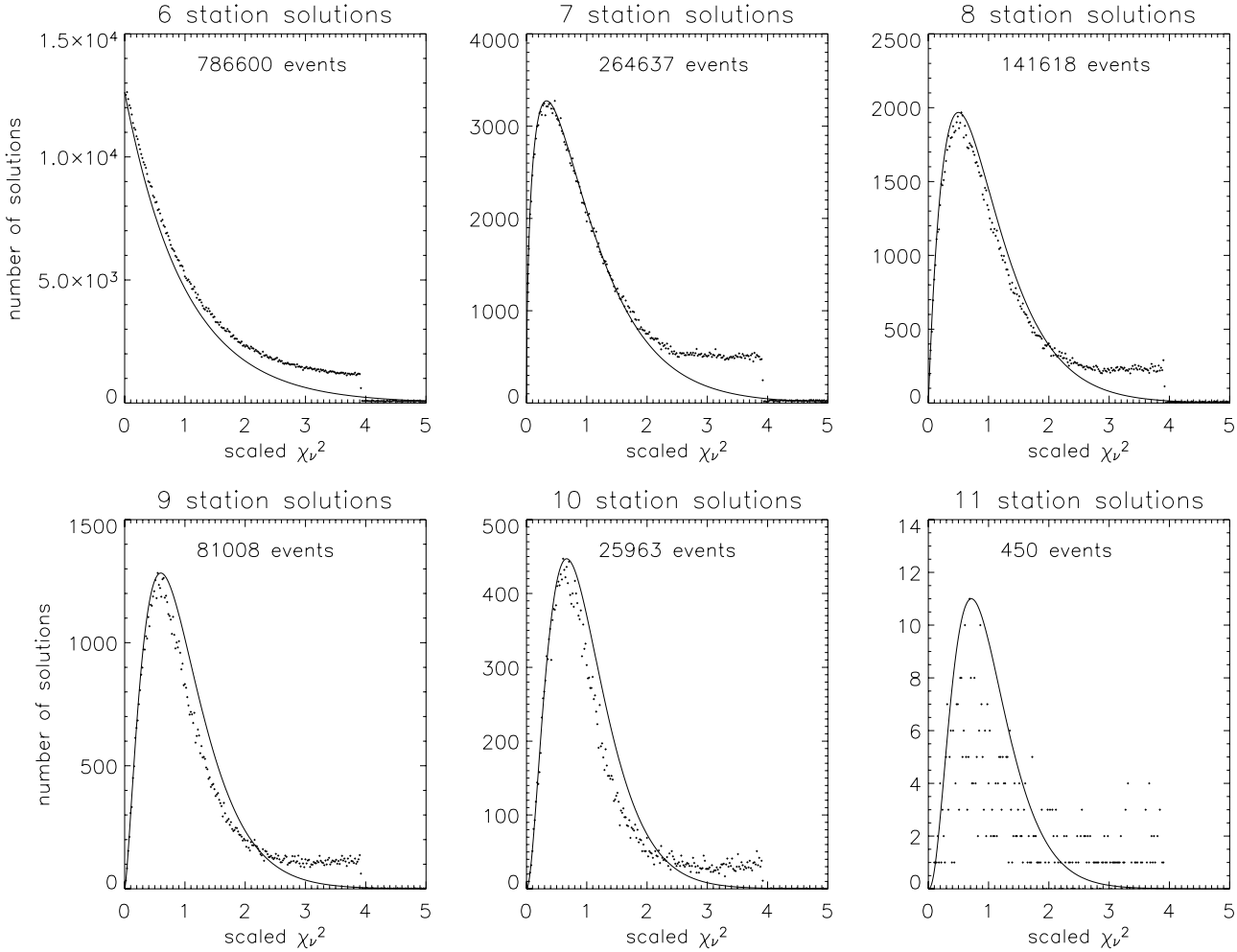

Figure 10. Same as Figure 9, except for 10 min of lightning data over the network on 11 June 2000. The timing uncertainty was slightly larger than for the deterministic balloon pulses, having an average value $\Delta t_{\rm rms}$ = 50 ns and varying from 53 ns for six station solutions, which are the most numerous for lightning sources, to 46 ns for ten station solutions. In addition, the distributions have an enhanced "tail" at larger chi-square values. The exact timing uncertainties vary somewhat from storm to storm and during a storm.

will always tend to be stations located transverse to and along the arrival direction.

4.1. Azimuthal Position

[42] For determining the azimuthal position of the source, one can assume to first order that the wavefront from the distant source is planar. Referring to Figure 11b, the azimuth angle ϕ is determined by the arrival times at the two ends of the transverse baseline, namely at stations S1 and S3. From the right triangle in the figure, one has that

$$D \sin\phi = c\, T_{3,1}, \tag{2}$$

where $T_{3,1} = T_3 - T_1$ is the difference in the arrival times at S3 and S1. For small ϕ the rms uncertainty in the azimuth angle is related to the rms uncertainty in the arrival time difference $T_{3,1}$ by $\Delta\phi = (1/D)c\,\Delta T_{3,1}$. The resulting uncertainty in the y direction is therefore

$$\Delta y = r\,\Delta\phi = \left(\frac{r}{D}\right) c\,\Delta T_{3,1}. \tag{3}$$

For equal timing uncertainties Δt at each station the rms uncertainty $\Delta T_{3,1} = \sqrt{2}\,\Delta t$. For Δt = 50 ns, $c\,\Delta T_{3,1}$ = 21 m. At a range of 100 km the azimuth uncertainty is 35 m rms for a 60 km diameter network typical of the LMA. The azimuth position is therefore well determined.

[43] In an actual network the azimuth angle will be found from the difference of the arrival times at a number of pairs of stations. However, the accuracy of ϕ will be determined primarily by stations having the greatest separation transverse to the incident signal.

4.2. Range Determination

[44] The range is obtained from the curvature of the wavefront reaching the network (Figure 11c). Closer events will have greater curvature; more distant events will have less curvature. To determine the curvature, we can assume to first order that the source lies on or above the x axis so that the wavefront reaches S1 and S3 at the same time. In addition, S0 is assumed to be halfway between S1 and S3. The difference $T_{13,0}$ between the arrival time at S1 and S3 and at S0 is a measure of the curvature and thus of the distance to the source.

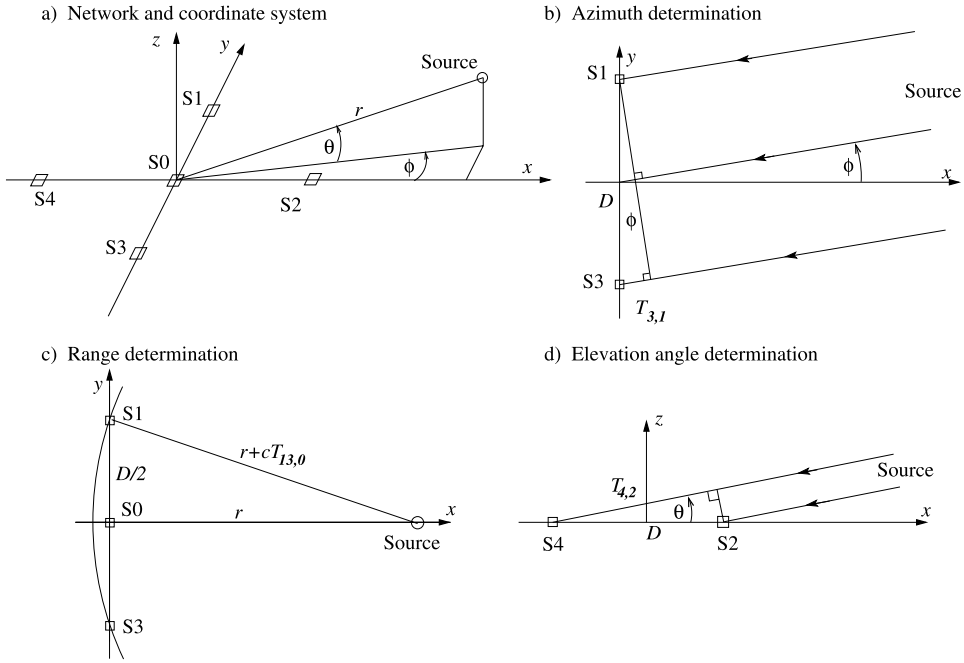

Figure 11. Simple model describing the fundamental way in which distant sources are located by a time of arrival (TOA) network. (a) Basic five station network consisting of three transverse stations (S0, S1, S3) and two longitudinal stations (S2, S4). Geometries for determining (b) the azimuth angle ϕ, (c) range r, and (d) elevation angle θ.

[45] From an analysis of the right triangle in Figure 11c the slant range r to the source is given by (see section C1)

$$r \simeq \frac{D^2}{8cT_{13,0}}, \tag{4}$$

and the rms uncertainty in r is

$$\Delta r \simeq 8\left(\frac{r}{D}\right)^2 c\Delta T_{13,0}. \tag{5}$$

The range uncertainty thus increases as the square of the range, scaled by the network diameter D. Although $T_{13,0}$ can be obtained by averaging the individual time differences $T_{1,0}$ and $T_{3,0}$, the resulting improvement in $\Delta T_{13,0}$ is relatively minor. For simplicity we therefore assume that the timing error for range is the same as for the azimuth determination, namely $\Delta T_{13,0} = \sqrt{2}\,\Delta t$. With this the range uncertainty is $\Delta r = 0.47$ km rms at 100 km distance from a 60 km diameter network.

[46] Equation (5) confirms *Boccippio et al.*'s [2001] empirical result that the range uncertainties increase as r^2. In addition, it determines the constant of proportionality of the increase in terms of the basic parameters of the network. Looking at the range determination from the curvature standpoint also provides a physical explanation for why *Koshak and Solakiewicz* [1996] found that a square network of four stations had blind regions in the directions of the edges of the square. For such a network, there is no central station to provide a measure of the wavefront curvature. Any network having one or two linear rows of stations would have a similar problem and could not accurately determine the distance to an event along the direction of the rows. A good network requires three or more widely spaced stations transverse to waves approaching from any direction. This is readily achieved in most networks.

4.3. Height Determination

[47] The elevation angle θ is determined from the arrival times at the longitudinal stations on the close and far sides of the network (Figure 11d). As in the azimuth determination, the incident wave can be assumed to be planar. For simplicity we consider measurements only at stations S2 and S4 and assume that the source is situated off the end of the S2–S4 baseline. For distant sources, θ will be small, and the arrival time difference $T_{4,2} = T_4 - T_2$ is only slightly less than the horizontal transit time between the two stations. The elevation angle is determined from the relatively small difference between $T_{4,2}$ and the transit time. Small errors in $T_{4,2}$ therefore produce relatively large errors in θ. This is a fundamental disadvantage of ground-based networks and results from the fact that such networks do not have significant vertical baselines.

[48] Assuming the distance between S2 and S4 is D, then from the right triangle in Figure 11d,

$$D\cos\theta = c\,T_{4,2}. \tag{6}$$

From this it is readily shown that the rms uncertainty in θ is

$$\Delta\theta = \frac{c\,\Delta T_{4,2}}{D\sin\theta} \simeq \frac{r}{D}\frac{c\,\Delta T_{4,2}}{z}, \tag{7}$$

where z is the height of the source above the plane of the network. (At large distances, z differs from the altitude h

above local ground due to the curvature of the Earth.) The corresponding uncertainty in the height is

$$\Delta z = r\Delta\theta = \frac{r^2}{D}\frac{c\,\Delta T_{4,2}}{z} = \Delta z_\theta. \quad (8)$$

As before, $\Delta T_{4,2} = \sqrt{2}\Delta t$. For an event at 10 km altitude and 100 km range the height uncertainty is 0.35 km rms for a 60 km diameter network. The height uncertainty is thus comparable to the range uncertainty (0.47 km).

[49] The above gives the contribution of the elevation angle uncertainty to Δz. An additional contribution comes from the fact that the range is also uncertain. The contribution of the range uncertainty to the height error is given by

$$\Delta z_r = \sin\theta\,\Delta r = \frac{z}{r}\Delta r = 8\frac{rz}{D^2}c\,\Delta T_{13,0}. \quad (9)$$

For a source at 10 km altitude and 100 km range, Δz_r is only 47 m rms for a 60 km diameter network and is thus small compared to the elevation contribution. As shown below, for typical lightning source heights, it can be shown that the range contribution is always less than the elevation contribution for large-diameter (e.g., 60 km) networks and beyond a certain range for smaller diameter (e.g., 15 km) networks.

[50] Except for the slight difference in the ΔT values, the contribution of the range uncertainty to the height uncertainty is given by

$$\Delta z_\theta = \frac{rD}{8z^2}\Delta z_r.$$

For a source at 10 km altitude and 100 km range, $\Delta z_\theta/\Delta z_r \simeq 1.9$ for a 15 km diameter network and $\simeq$7.5 for a 60 km diameter network. The contributions would be equal when $rD \simeq 8z^2$. For a source at 10 km altitude, this occurs at $r \simeq 53$ km for a 15 km diameter network, with the elevation contribution being greater for $r > 53$ km and less for $r < 53$ km. For a 60 km diameter network the contributions would be equal at a range $r \simeq 13$ km, which is smaller than the network radius. By requiring that $r \geq D$, networks larger than about $D \simeq \sqrt{8}z = 28$ km in diameter will always have the elevation contribution to the height error exceed the range contribution for sources at or below 10 km altitude. Because the two contributions to the height error are essentially uncorrelated, the total altitude uncertainty will be the quadrature sum of Δz_θ and Δz_r.

[51] In an actual network the elevation angle will be determined primarily by the stations with the greatest separation along the direction to the source.

4.4. Summary

[52] Assuming that the pairwise timing uncertainties ΔT are the same for the azimuth, range, and height determinations, and neglecting the range contribution to the height uncertainty, the model results for the location uncertainties of sources outside the network are approximately given by

$$\Delta y = \left(\frac{r}{D}\right)c\,\Delta T, \quad (10)$$

$$\Delta r = 8\left(\frac{r^2}{D^2}\right)c\,\Delta T, \quad (11)$$

$$\Delta z = \left(\frac{r^2}{Dz}\right)c\,\Delta T, \quad (12)$$

where $\Delta T \simeq \sqrt{2}\,\Delta t$ is the uncertainty in the time difference of arrivals at pairs of stations and Δt is the rms timing uncertainty at each station. As determined in section 3, the location uncertainties for sources over the network are given approximately by

$$\Delta d = \frac{1}{\sqrt{2}}\,c\,\Delta t = \frac{1}{2}c\,\Delta T \quad (13)$$

$$\Delta z = \left(\frac{d+r}{z}\right)c\,\Delta t = \frac{1}{\sqrt{2}}\left(\frac{d+r}{z}\right)c\,\Delta T, \quad (14)$$

where d is the distance to the closest station. Thus the location errors all scale to $c\,\Delta T$ but with different constants of proportionality in each case. For $\Delta t = 50$ ns, characteristic of the STEPS network, $c\,\Delta T = 21$ m.

[53] Figure 12 shows plots of the location uncertainties as a function of range for sources outside the network used during STEPS. The predicted uncertainties from the simple models of Figure 11 are compared with those obtained from a covariance analysis of the complete thirteen station network. This is done for sources at 10 km altitude in E–W and N–S vertical planes through the network centroid. The models predict that the range and altitude uncertainties increase as r^2, while the azimuth uncertainty increases only as r. The covariance results confirm this, showing that the range errors increase parabolically with distance, while the azimuth errors increase linearly. (The constants of proportionality are somewhat different in each case, as discussed below.) The difference in the power law dependence for the range and azimuth determinations occurs because range is determined from a second-order measurement (of the wavefront curvature), while the azimuth requires only a first-order measurement (of the arrival direction of a planar wavefront). This causes the azimuth uncertainty at a given distance from the network to be small compared to the range uncertainty. On the other hand, the range and altitude uncertainties both increase as r^2 and, for the STEPS network, are comparable to each other. From equation (12) the constant of proportionality for the height uncertainty increases as $1/z$ so that Δz is larger for sources at a lower height above the network horizon than at higher height. For the $\simeq$60 km diameter STEPS network and 10 km source heights the constants of proportionality for the range and altitude uncertainties were about the same.

[54] Note that the relative magnitudes of the location uncertainties in distant storms can be obtained from equations (10)–(12) by expressing Δr in terms of Δy and Δz. This gives

$$\Delta r = \begin{cases} 8\left(\frac{r}{D}\right)\Delta y \\ 8\left(\frac{z}{D}\right)\Delta z\,. \end{cases}$$

The range error Δr exceeds the azimuth error Δy for $r > D/8$ (i.e., for any location outside the network), and the radial distortion of the sources continues to increase as r gets larger. For a source at 100 km range, $\Delta r/\Delta y \simeq 13$ for a 60 km diameter network and $\simeq$53 for a 15 km diameter network. Distant storms therefore are elongated radially, an obvious feature of actual observations (e.g., Figure 15). The radial exaggeration is greater for a small-diameter network than for a large network. On the other hand, the ratio of the range

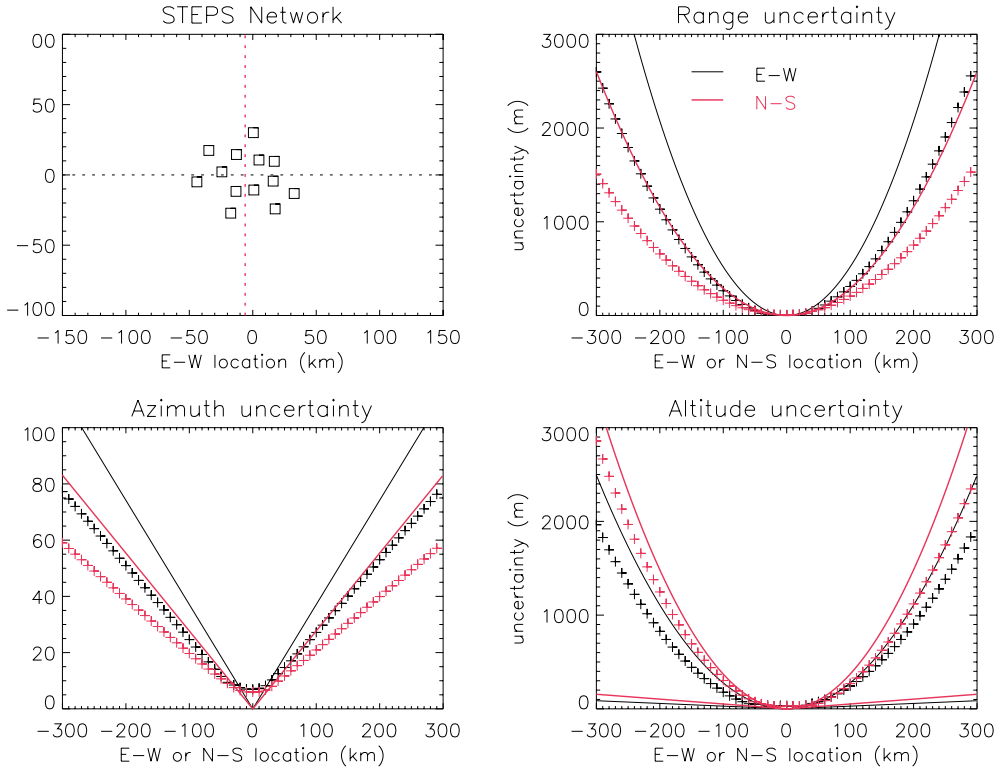

Figure 12. (top right) Range, (bottom left) azimuth, and (bottom right) altitude uncertainties of (top left) the STEPS network for sources at 10 km altitude in E–W (black) and N–S (red) vertical planes through the network centroid. The plus symbols show the covariance error estimates for the complete 13 station network, assuming a timing uncertainty of 50 ns rms. The solid lines show the error estimates from the simple model of Figure 11 for 50 ns timing error and network sizes D = 78 km and 57 km in the E–W and N–S directions, respectively. The model-predicted errors are larger than the covariance values due to averaging effects when all stations are assumed to participate in the solutions (see text). The contribution of the elevation angle and range uncertainties to the altitude error are shown separately in the altitude panel. The approximate network centroid was determined by minimizing the azimuthal error for sources in the E–W and N–S directions and was at (x, y) = (−6, 0) km relative to the coordinate origin.

and height errors is $8z/D$ and depends on the source height and not on range. The STEPS network was 60–80 km in diameter so that sources at z = 7.5–10 km altitude would have approximately equal range and height uncertainties.

[55] The STEPS network had a larger extent in the E–W direction than in the N–S direction, with the N–S extent being 57.2 km and the E–W extent being 76.6 km. Since the range and azimuth errors depend on the transverse extent, while the altitude error depends on the longitudinal extent, the range and azimuth uncertainties in Figure 12 are greater for sources in the E–W plane (black) than for sources in the N–S plane (red). The inverse is true for the altitude uncertainty. In all cases the covariance errors are less than those predicted by the simple model, assuming that D corresponds to the physical extent of the network in the appropriate direction. This reflects the effect of averaging the results of a number of baselines when data from all stations are used to locate an event. Stated another way, fully overdetermined solutions correspond to an effective network diameter larger than the physical diameter. By matching the model predictions to the covariance results, the effective size of the thirteen station network was D = 78 km in the N–S direction and 100 km in the E–W direction. The effective dimensions of the complete STEPS network were therefore 36% and 31% greater than its physical dimensions. (Another interesting feature of the Figure 12 results is that the difference between the model- and covariance-predicted errors is less for the altitude determination than for the range and azimuth locations. This indicates that the altitude determination is less affected by averaging and therefore that it is determined primarily by the closest and most distant stations of the network (or of the set of stations that participate in a given solution).)

[56] Rather than being located by all stations of a network, radiation events are invariably located by only a subset of stations (e.g., Figures 9 and 10). This counteracts the tendency of the network to be oversized by multiple-station averaging. The net effect is that the effective diameter might be comparable to (or smaller than) the actual diameter, making the simple model estimates approximately correct when the actual diameter is assumed.

5. Further Comparison With Experimental Observations

[57] In this section we use observations of aircraft tracks and of distant storms to gain additional insights into the

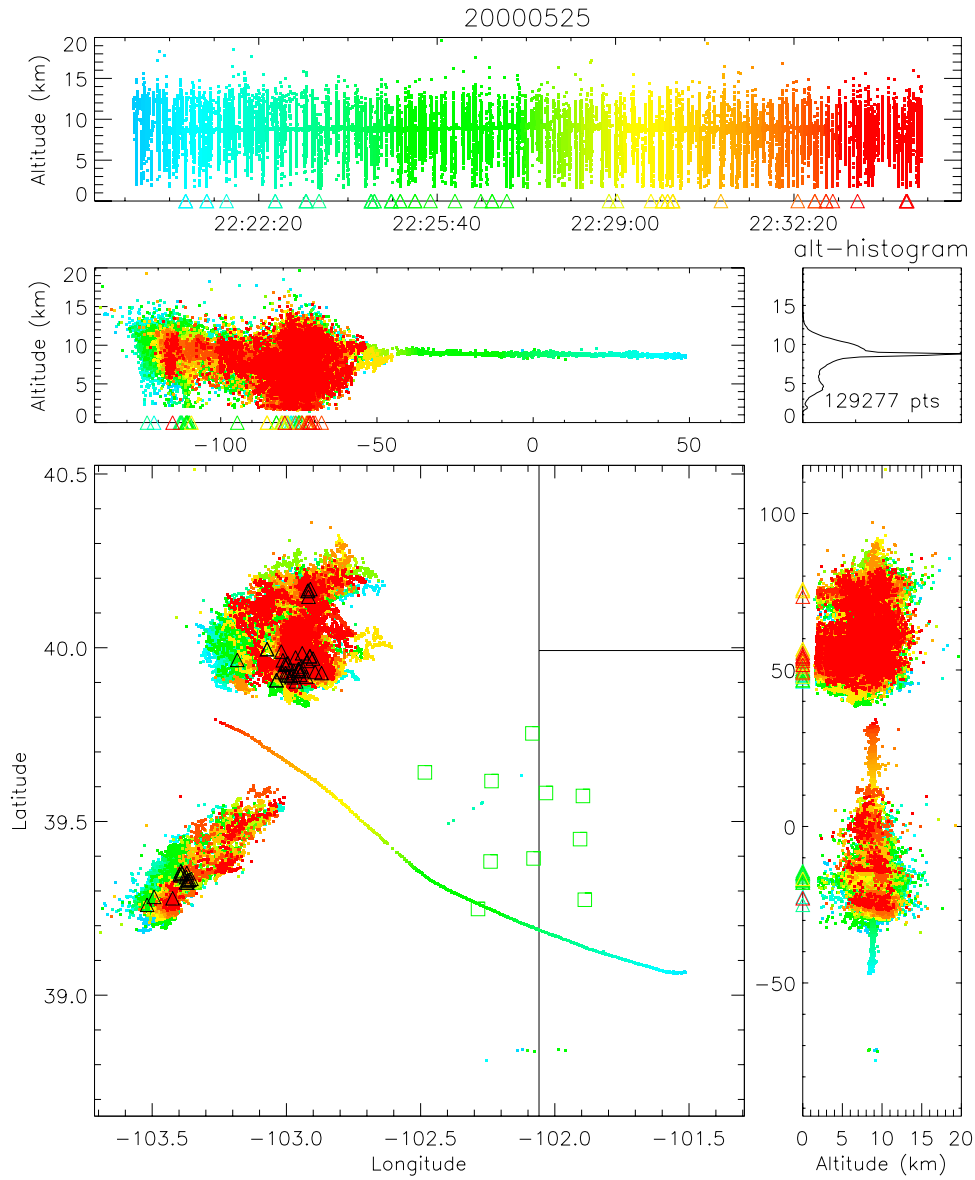

Figure 13. Aircraft track over Kansas and Colorado on 25 May 2000. The plane was flying from east to west at about 9 km altitude (29.5 left) and vectored between two electrically active storms. The airplane was tracked by the LMA because it was flying through an ice crystal cloud downwind of the storms that caused it to become charged and give off a steady stream of small sparks. The plane was tracked for 13 min over a 170 km distance and was presumably a commercial aircraft. Two other aircraft were more weakly detected over the center and to the south of the mapping network. The squares indicate the operational stations on this day; only sources located by seven or more stations are shown. The triangles indicate the location of negative polarity ground discharges. The distance scales are in latitude and longitude in the plan view and in kilometer units in the vertical projections.

performance of the mapping network and to test the validity of the error models.

5.1. Aircraft Tracks

[58] On a number of occasions during STEPS the mapping array located aircraft flying over or near the project area. Visual observations showed that the aircraft were detected when ice crystal clouds (cirrus clouds or storm anvils) were present over or around the network. From this, it was evident that the LMA was locating small sparks caused by collisional charging from the planes as they flew through the ice clouds. That such charging occurs is well known [e.g., *Gunn et al.*, 1946; *Illingworth and Marsh*, 1986; *Jones*, 1990]. Sparking has also been detected by the LDAR system from aircraft flying through cirrus clouds [e.g., *Maier et al.*, 1995]. Because airplanes fly along straight paths, the tracks can be used to investigate the location uncertainties by measuring the scatter of the sources along the track. This approach was used to determine the errors of the original LDAR system, as discussed in section 1.

[59] Figure 13 shows an example of an aircraft track observed on 25 May 2000. Only 10 stations were operating

on this day, which was the first day data were recorded during STEPS. The airplane was flying from east to west downwind of a line of thunderstorms in eastern Colorado. The speed (245 m s^{-1} or 550 mph) and altitude of the track are typical of a commercial airliner. As it flew westward, the aircraft gradually ascended from 8.5 km to 9.0 km altitude (28–29.5 left) and vectored through the gap between two thunderstorms. After passing between the storms the track ended as the plane presumably emerged into cloud-free air. More than 300,000 sparks were located over the 800 s (13 min) duration of the track. Two weaker tracks are also seen in Figure 13, south of and over the center of the network.

[60] Figure 14 shows the standard deviation of the scatter about the mean track and compares the scatter with the covariance estimates of the location uncertainties. Separate plots are shown for the E–W, N–S, and altitude errors. The standard deviation of the scatter (red plusses) was determined relative to a cubic spline fit to the track and is smoothed by a 13 s (3.2 km) running average. The black dots indicate the covariance values for the individual events, assuming 50 ns rms timing errors. As in Figure 7, the dots group into multiple sets of curves corresponding to different sets of stations being involved in the solutions. The average of the covariance results is shown by the set of green dots and should correspond to the observed scatter. The two are often in good agreement, but the scatter is sometimes larger than would be predicted by the average covariance value. The set of orange points at the bottom of each plot is the covariance error if all stations contributed to the solutions and should represent the lower limit of the location uncertainty. This is indeed the case: Some station combinations come close to achieving the lower limit, and the measured scatter sometimes achieves it as well.

[61] In the first half of the track the airplane flew toward, over, and past the southern part of the network. During this time the E–W error decreased from 200 m rms to almost 10 m and then increased again (Figure 14 (top)). The minimum error occurred at 320 s; at this time the airplane was at $x = -2$ km, i.e., almost due south of the coordinate origin near the center of the network. (The minimum transverse error location provides a means of defining the centroid of the network in a given direction. The covariance analyses of Figure 12 showed that when all stations were incorporated into the calculations, the network centroid was at $x, y = (-6, 0)$ km relative to the coordinate origin. The Figure 14 results for the 25 May airplane track indicate that the network centroid was at about $(-2, 0)$ km for the 10 stations that were operational on that day.) The E–W scatter agreed well with the predicted covariance values up through the time of the minimum but became more erratic for about 300 s afterward.

[62] The N–S error (Figure 14 (middle)) had a broader and shallower minimum at about 575 s as the airplane passed due west of the coordinate origin. The covariance minimum was only partially reflected in the observed scatter, probably because the sparks were weak and even dropped out during this time (shown later in Figure 17).

[63] The altitude uncertainty (Figure 14 (bottom)) showed two local minima as the airplane passed over the southern edge of the network. The first minimum, at about 200 s in Figure 14, occurred as the airplane approached station ''J'' on the southeast edge of the network. The second minimum (at 400 s) occurred as the airplane passed over the southwestern station ''G.'' The airplane passed within 14 km horizontal distance of station J and 2 km horizontal distance of G. The altitude scatter agreed reasonably well with the predicted covariance values while approaching and passing J but did not agree very well with the covariance values during the G overpass. Rather, during the G overpass the scatter exhibited large fluctuations and even had a relative maximum at the time of the covariance minimum. The latter may have been caused by decreases in the signal strength as the plane passed close to the null of station G's receiving antenna. (The first minimum in the altitude error along the 25 May airplane track occurred not at the time of closest approach to Station J, which was at $x = +12$ km in Figure 13, but earlier, when the plane was at $x \simeq +25$ km. At this time the plane was off the end of the baseline between J and the network centroid. From the results for altitude determination (Figures 11d and 22b) the network had the greatest longitudinal (as opposed to transverse) extent at the time of the minimum altitude error. This is consistent with a visual inspection of the network in Figure 13 and with the position of the airplane at the time of the minimum.)

[64] During the final part of the track, from 600 s on, the observed scatter (red) and average covariance values (green) agreed well in each direction. The individual covariance values for the E–W and N–S errors showed a bimodal distribution, with one of the modes giving close to the optimal accuracy and the other mode having errors that were 2–5 times larger. The average covariance values and the scatter tracked the mode having the larger errors, indicating that most of the sparks during this time were located by a less than optimal set (or sets) of stations. The bimodal behavior was not present in the vertical errors, indicating that the bimodality resulted from inclusion or loss of stations along transverse (N–S) baselines.

[65] Figures 15 and 16 show data for another track, in this case, for an aircraft flying from west to east at 10–11 km altitude (33–36 left), 85–120 km northeast of the network. Good agreement is obtained between the observed scatter and the covariance error results. At 100 km range, approximately in the middle of the track, the observed height scatter was between 400 and 500 m rms, slightly less than the average covariance result (green dots) and slightly greater than the optimal, all-station covariance prediction (of about 300 m). (At 100 km range the model-predicted uncertainty is about 370 m rms.) The range errors are discussed later and also agree with the model prediction.

[66] Note that comparing Figures 14 and 16 for the two aircraft tracks shows that while the optimal covariance-predicted uncertainties (orange dots) varied in a steady manner with time in both cases, the individual and average covariance values (black and green dots) as well as the measured scatter of the source locations fluctuated considerably during the 25 May track. Further examination of the observations indicates that this

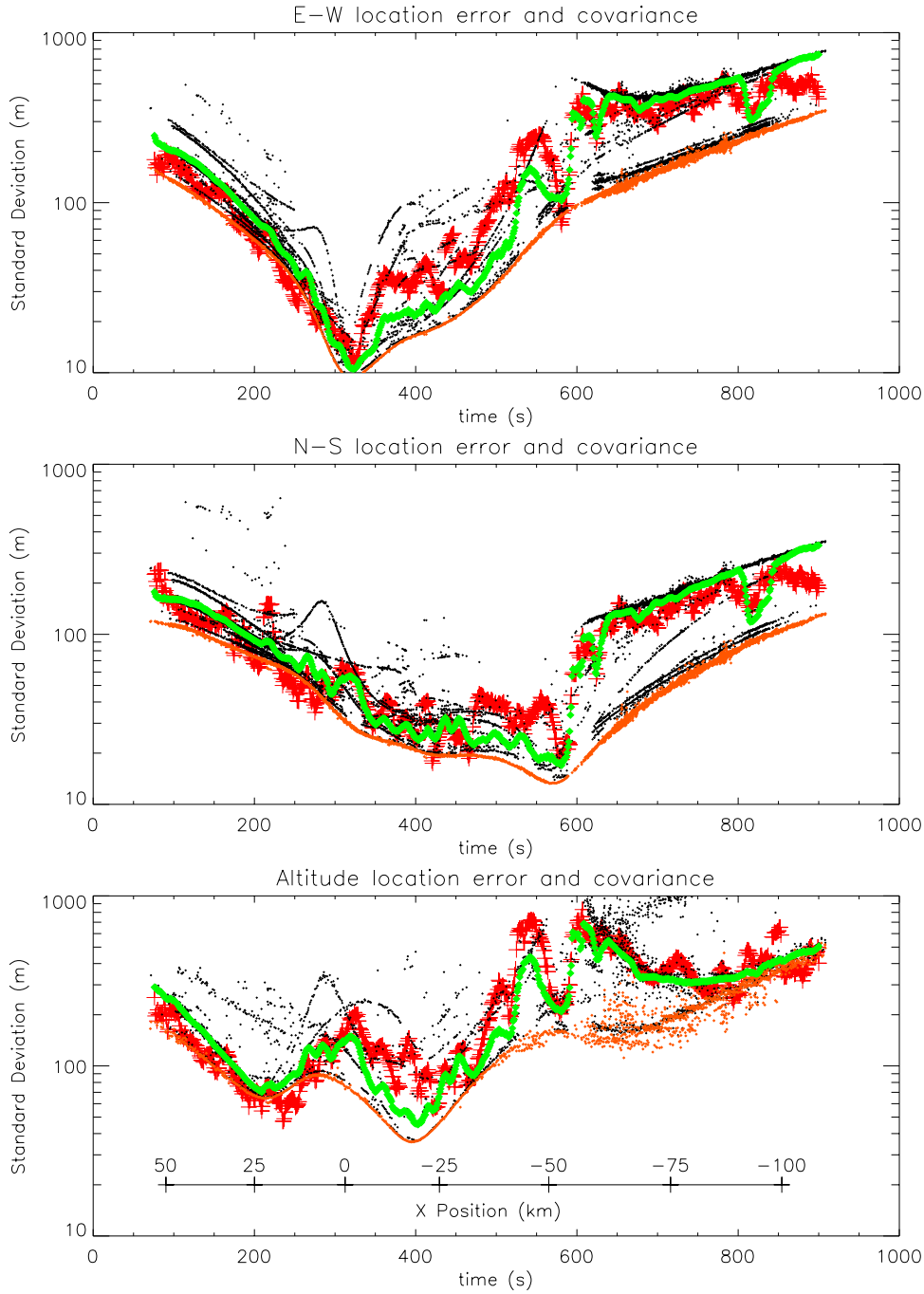

Figure 14. Measured and predicted rms scatter of the radiation sources in three Cartesian directions about the mean of the 25 May aircraft track. Shown are the standard deviation of the observed scatter (red), the covariance error estimates for each individual spark (black dots, assuming 50 ns rms timing uncertainty), and a running average of the covariance values (green), for all events located by six or more stations. The orange dots show the covariance values if all 10 stations operational on that day had located the events and represent the optimal error. The individual covariances group into sets of curves corresponding to different combinations of stations, as in Figure 7, some of which approach the optimal error. The predicted error in altitude shows two minima as the plane passed over or close to the two southern stations of the network. The x and y errors have minima due south and west of the network center, respectively.

resulted from 25 May being the first day data were recorded during STEPS and from relatively large differences in the threshold values for recording data at each station (Appendix A). The remaining stations of the network and the communications links between stations were still being set up on 25 May, and we had not yet started monitoring and adjusting or equalizing the threshold values. The performance difference is also seen in

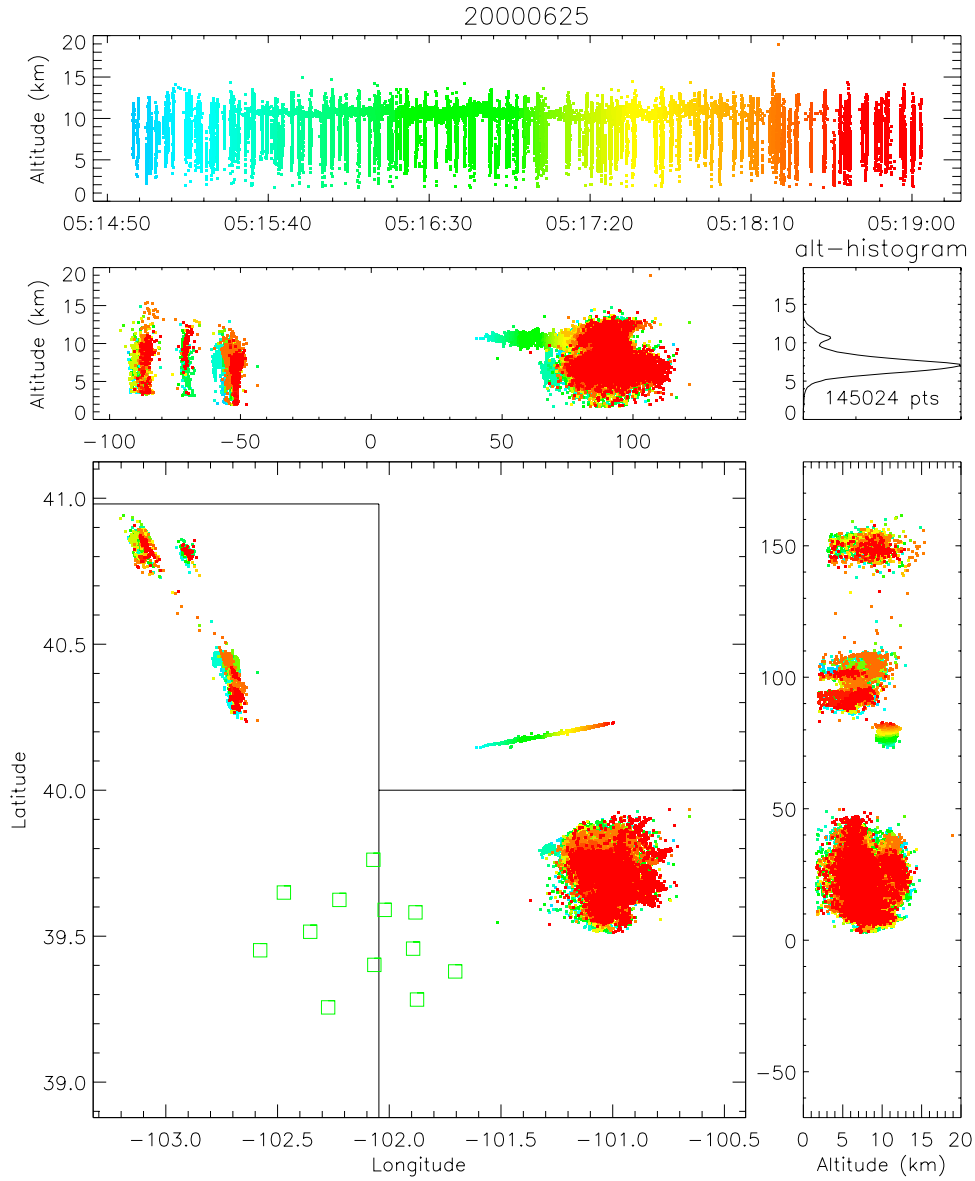

Figure 15. Track of an aircraft heading east over Nebraska on 25 June 2000. The airplane was about 100 km northeast of the center of the mapping network. The black lines in the plan view of this and other figures indicate state lines of Kansas, Colorado, and Nebraska. Note the radial elongation of the distant storms NNW of the network. Only sources located by seven or more of the 12 active stations on this day are shown.

range errors for the two tracks, summarized in Figure 20, wherein the 25 May observations (diamonds) corresponded to a smaller effective network diameter than the 25 June observations (triangles). The fact that the network functioned as well as it did on 25 May attests to the robustness of TOA measurements.

[67] Figures 17 and 18 show the rate of sparking and the source powers for each of the airplane tracks. The sparking rate (top panels) is determined by differencing the times between successive events and involved no averaging. The rate indicates two modes of discharging: a periodic or regular mode and an aperiodic or irregular mode. The periodic mode exhibits a characteristic "fringing" pattern caused by sparks sometimes being missed by the system. The upper fringe corresponds to each spark of a periodic sequence being located. When one spark was missed between successive located events, the time between events was doubled and the apparent frequency was therefore halved, giving rise to the second fringe. Similarly, the third fringe corresponded to two sparks being missed between successive detections, etc. The actual sparking rate therefore corresponds to the top fringe and was about 100 s^{-1} during the first half of the 25 May track and close to 200 s^{-1} during the final half of the 25 June track. The irregular mode was characterized by the lack of fringing; during these times the sparking occurred at rates up to 1–10 kHz for both airplane tracks and also had higher source powers. In the 25 May track the irregular mode had a sudden onset as the plane got closer to the storms. This, coupled with the increased rate and higher source

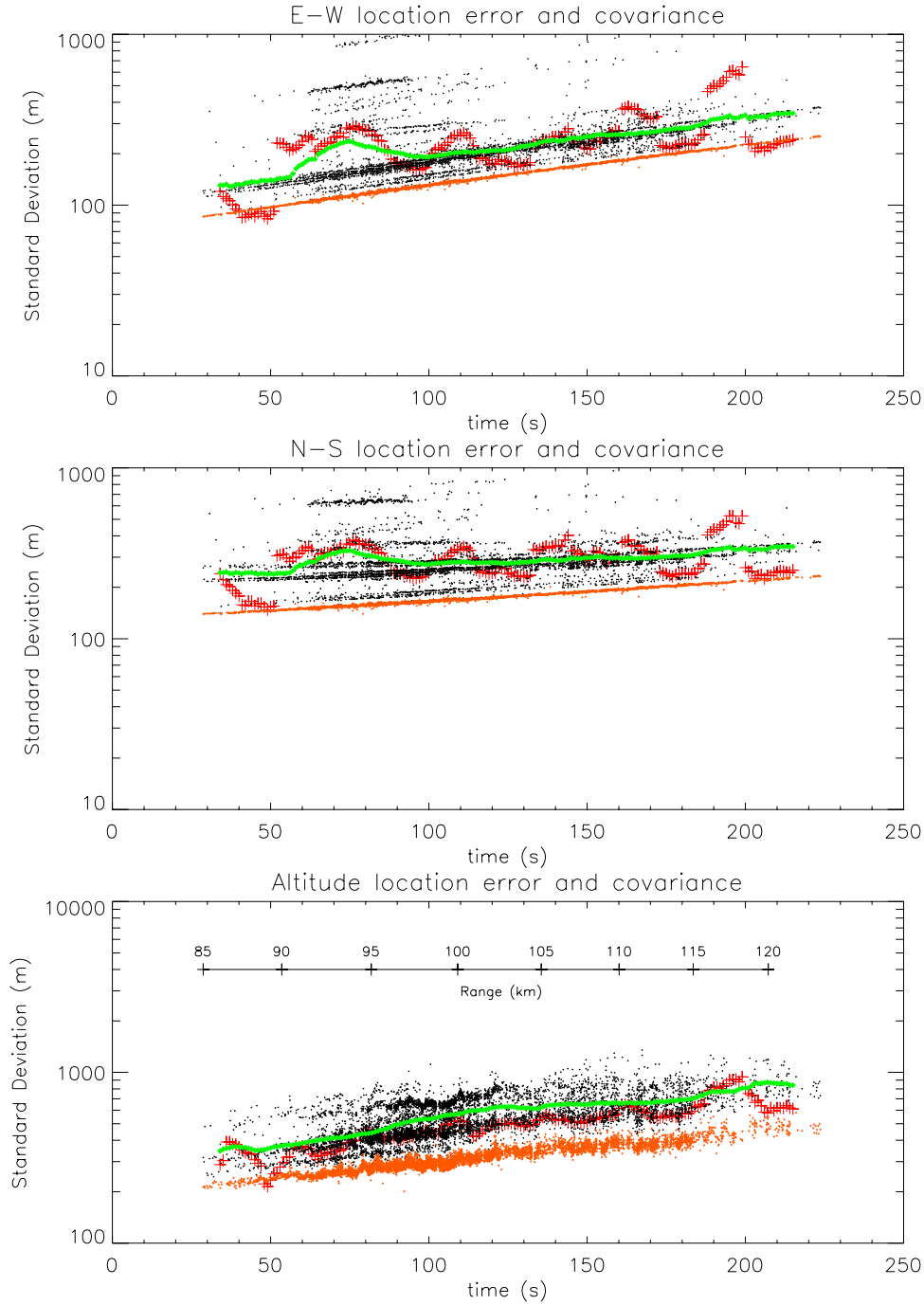

Figure 16. Same as Figure 14, but for the 25 June track and for all events located by six or more stations. The measured scatter (red) agreed well with that predicted by the average of the covariance values (green), but this was somewhat greater than the optimal error (orange) due to the plane's distance, which caused the sparks to be detected by relatively small numbers of stations.

powers, indicates that the plane had entered a more dense ice crystal region, presumably the actual anvil cloud of the storms.

[68] The detected source powers (bottom panels) ranged from 0.3 W up to about 3 W for the 25 May track and from 2 to 5 W for the more distant 25 June track. The lower envelope of the values reflects the minimum detectable source power of the network. In the 25 May track the minimum detectable power varied in an approximate parabolic manner as the plane approached and then receded from the network.

[69] The fact that the source powers of the aircraft sparks were close to the minimum detectable values would have increased the errors in the TOA measurements above the 50 ns values assumed in the covariance analyses. The average covariance errors therefore represent a lower bound for the observed scatter, as sometimes seen in the 25 May data. In Appendix B we show that in addition to random

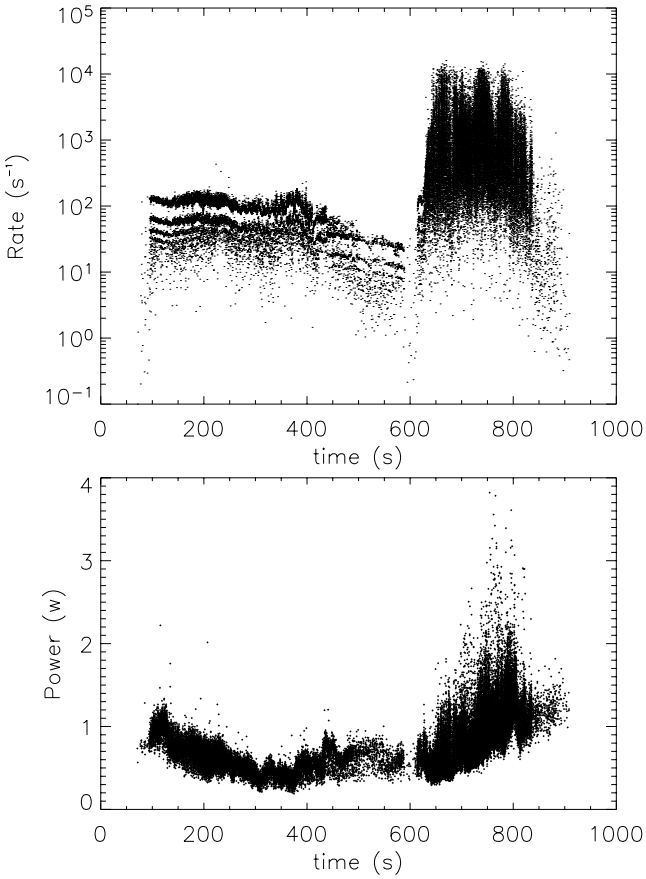

Figure 17. (top) Rate of detected sparks and (bottom) radiated source power as a function of time during the 25 May airplane track. The fringing pattern in the rate plot results from some sparks of a periodic sequence not being located by the system (see text).

errors, the airplane tracks had systematic sawtooth errors (Figure B1) that would have been partially responsible for the fluctuations in the scatter about the mean track.

5.2. Distant Storm Observations

[70] Observations of distant localized storms provide another way of estimating the range errors of the system. As seen in Figure 15, the extent of the lightning sources in distant storms is elongated radially relative to their azimuthal extent. The radial spread of the sources can be measured relative to their azimuthal spread to estimate the range uncertainty. Similar measurements were used by *Boccippio et al.* [2001] to estimate the range error of the LDAR system.

[71] An analysis of the radial and azimuthal variances of the sources due both to the storm size itself and to the location errors (see section C2) shows that if the parent storm itself is circular or nearly circular,

$$\sigma^2_{\text{range}} \simeq \sigma^2_{\text{radial}} - \sigma^2_{\text{transverse}}. \tag{15}$$

In other words, the inferred variance of the range errors, σ^2_{range}, is the measured radial variance of the sources, σ^2_{radial}, reduced by the measured azimuthal (transverse) variance of the storm, $\sigma^2_{\text{transverse}}$.

[72] The result assumes that the azimuthal errors are small compared to the range errors, which is true for distant storms. If it cannot be assumed that the storms are circular (which is often or even usually the case), the result will apply to averages over a number of storms:

$$\langle\sigma^2_{\text{range}}\rangle \simeq \langle\sigma^2_{\text{radial}}\rangle - \langle\sigma^2_{\text{transverse}}\rangle\ . \tag{16}$$

The assumption here is that there is no systematic dependence of storm orientation in the set of storms being averaged.

[73] Observations of 60 localized storms at ranges greater than about 100 km have been used to estimate the rms range error σ_{range}. Figure 19 shows the measured radial and transverse spreads for each storm and the corresponding range error from equation (15). Seven out of 20 storms between 100 and 170 km range had negative apparent values of σ_{range}; since this is impossible, the storms in question could not have had a circular shape. At these distances the model-predicted range error is <1.5 km rms and does not significantly distort the storm so that noncircular shapes can easily dominate the results. Accordingly (and somewhat arbitrarily), we limited the analyses to the 40 storms beyond 170 km range and used equation (16) to estimate σ_{range}. The averaging was done over eight groups of four to six storms in each range bin, with the storms in

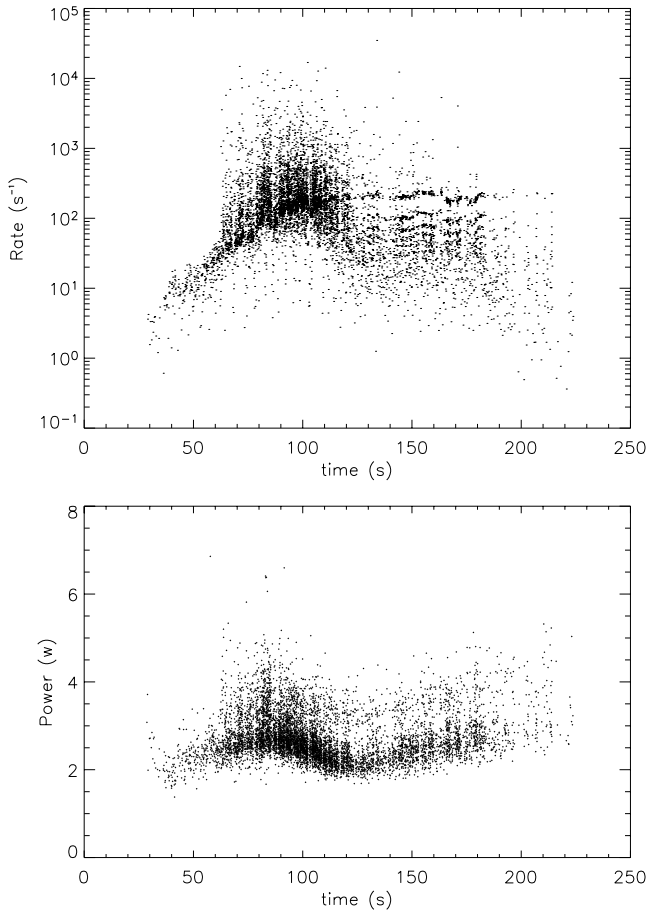

Figure 18. Same as Figure 17, except for the 25 June airplane track.

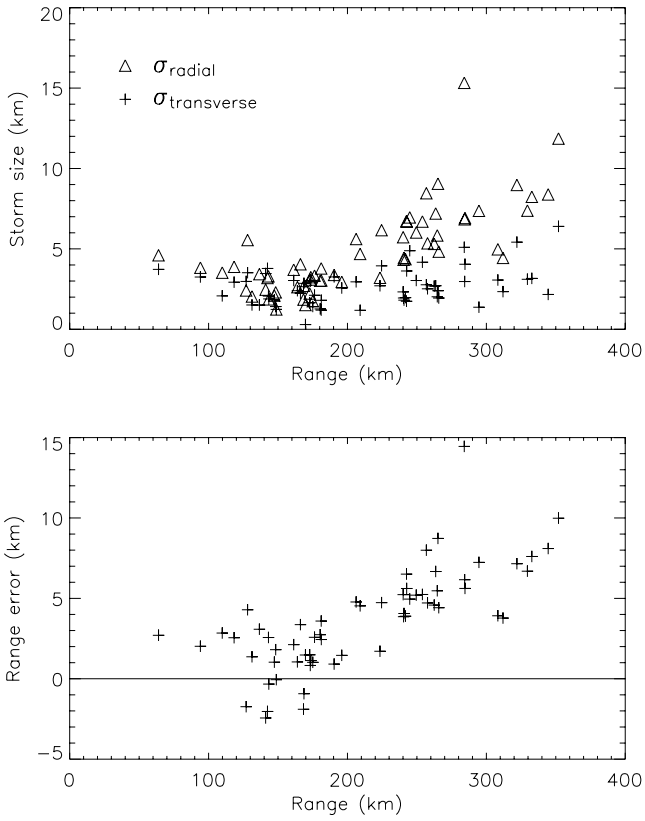

Figure 19. (top) Standard deviation of the lightning sources in distant localized storms in the radial and transverse directions and (bottom) the inferred rms radial range error. The negative range errors at <175 km range are not physically possible and indicate that the storms had unequal transverse and radial extents.

each group being in different directions from the network. The results are presented in section 5.3.

5.3. Summary of Range Errors

[74] Figure 20 summarizes the estimated range errors and compares the results with the simple model predictions for distant storms. The graph is presented in the same log-log form as Figure 6 of *Boccippio et al.* [2001] (hereinafter referred to as B2001) for comparison with their results. The straight lines in the figure correspond to the r^2 range dependence predicted by the simple model. The bottom two lines show the model-predicted range errors from equation (5) for network diameters D = 45 km and 70 km and for 50 ns rms timing errors, representative of the STEPS network. The estimated range errors from the distant storm analyses are shown by the square symbols and the estimated errors from the two aircraft tracks are shown by the diamond and triangle symbols. The data points typically lie between the two lines, indicating that the effective network diameter was between 45 and 70 km. The effective diameter corresponds to the transverse extent of the network and is reduced from the actual diameter by the fact that most radiation sources were located by only six or seven stations of the thirteen station array. The distant 25 June airplane track (triangles) corresponded to the largest effective diameter of about 70 km. The slightly larger uncertainties and smaller inferred network diameter for the 25 May airplane track (diamonds) likely resulted from the network not being fully operational on that day.

[75] The upper three lines and the plus symbols in Figure 20 are from Figure 6 of B2001 and describe the inferred range errors for the 16-km-diameter LDAR network at Kennedy Space Center. The dashed line is the rms error inferred by B2001 from aircraft measurements presented by *Maier et al.* [1995]. The aircraft data were obtained out to about 35 km range, mostly off scale to the left in Figure 20. B2001 characterized the range error by its rms value at 100 km distance; extrapolated to this distance, the range error from the aircraft data was σ_{100} = 3.6 km. (For comparison, σ_{100} = 0.35 km and 0.84 km for 70 km and 45 km effective diameters of the STEPS network, respectively.) Letting D = 16 km in equation (5), σ_{100} = 3.6 km gives $\Delta T_{13,0}$ = 38 ns for the rms timing error of the LDAR system. (*Maier et al.* [1995] reported that the aircraft location errors were consistent with 50 ns rms timing uncertainty; the range errors inferred by B2001 refine this result.) For comparison, the equivalent timing uncertainty of the LMA for deterministic transmitter pulses was Δt = 43 ns rms at a

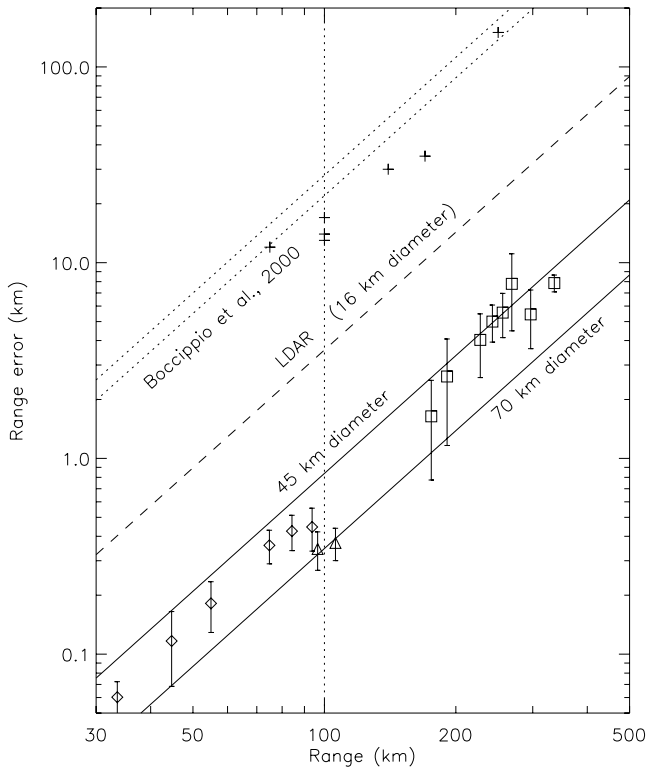

Figure 20. Standard deviation of the range error versus range outside the measurement network, showing the model-estimated performance of 70 km and 45 km diameter networks (two bottom lines), the errors estimated from localized storms at distances >150 km from the network center (open squares, representing averages over four or five storms grouped in range), and error estimates from the aircraft tracks of Figures 14 and 16 (diamonds and triangles, respectively). The top three lines and the data points denoted by the plus symbols are from *Boccippio et al.* [2001] and describe the inferred performance of the LDAR system at Kennedy Space Center (see text).

given station and $\Delta T = \sqrt{2}\Delta t = 61$ ns for time differences of arrival. Because the LDAR system digitized all the signals at the central station in exact time synchronization, it would be expected to have smaller relative timing errors than independent digitizing of the LMA. Despite its relatively small size, the LDAR network provided reasonably accurate range determinations out to at least 35 km range and, by extrapolation, to more than 100 km range.

[76] At distances greater than about 70 km, however, B2001 inferred that the range errors of the LDAR system were significantly larger than would be expected from the aircraft measurements. This was determined from the radial spread of sources in storms beyond 75 km range, indicated by the plus symbols in Figure 20. B2001's estimates did not attempt to account for storm size, however, and therefore overestimated the actual range errors by an unknown amount. The dotted lines in the upper part of Figure 20 are the range errors that B2001 determined would be needed to explain the systematic increase in the height of sources with distance from the LDAR network. The range errors inferred from the analysis had σ_{100} values of 22 and 28 km rms, a factor of 6–8 larger than expected from the aircraft measurements and somewhat larger than the distant storm values. From equation (4), in order to explain a σ_{100} value of 22 km, the rms timing uncertainty would have had to increase by a factor of 6, to 230 ns rms. Alternatively, the transverse diameter of the network would have had to be decreased by a factor of $\sqrt{6} = 2.45$ to an effective value of $D = 6.5$ km.

[77] Appendix B describes the effect of systematic errors upon the location accuracy and performance of the LMA. This analysis provides a simpler explanation for the systematic height errors of the LDAR data as being due to relatively small, systematic errors in the elevation angle determination rather than to overly large range errors.

6. Comparison to Hyperbolic Geometry

[78] In this section we relate the simple geometric models of this study to the geometry of hyperbolic formulations for TOA measurements. The formulations themselves are described by *Proctor* [1971] and are not repeated here. As discussed by Proctor and briefly described in Appendix A, the time differences of arrival (TDOA) at pairs of stations constrain the source to lie on hyperboloids of revolution about the baselines between pairs of stations. The three-dimensional location of the source is determined from the intersection of three or more such hyperboloids obtained from four or more stations.

[79] Figure 21a illustrates how stations locate the plan position of a source over the network. A cross-shaped network is used to do this. Four sets of hyperbolae are shown to indicate how the time differences of arrival at different pairs of stations determine the source location and the uncertainty in the location. For each station pair (e.g., 2–3), two hyperbolae are shown which indicate the

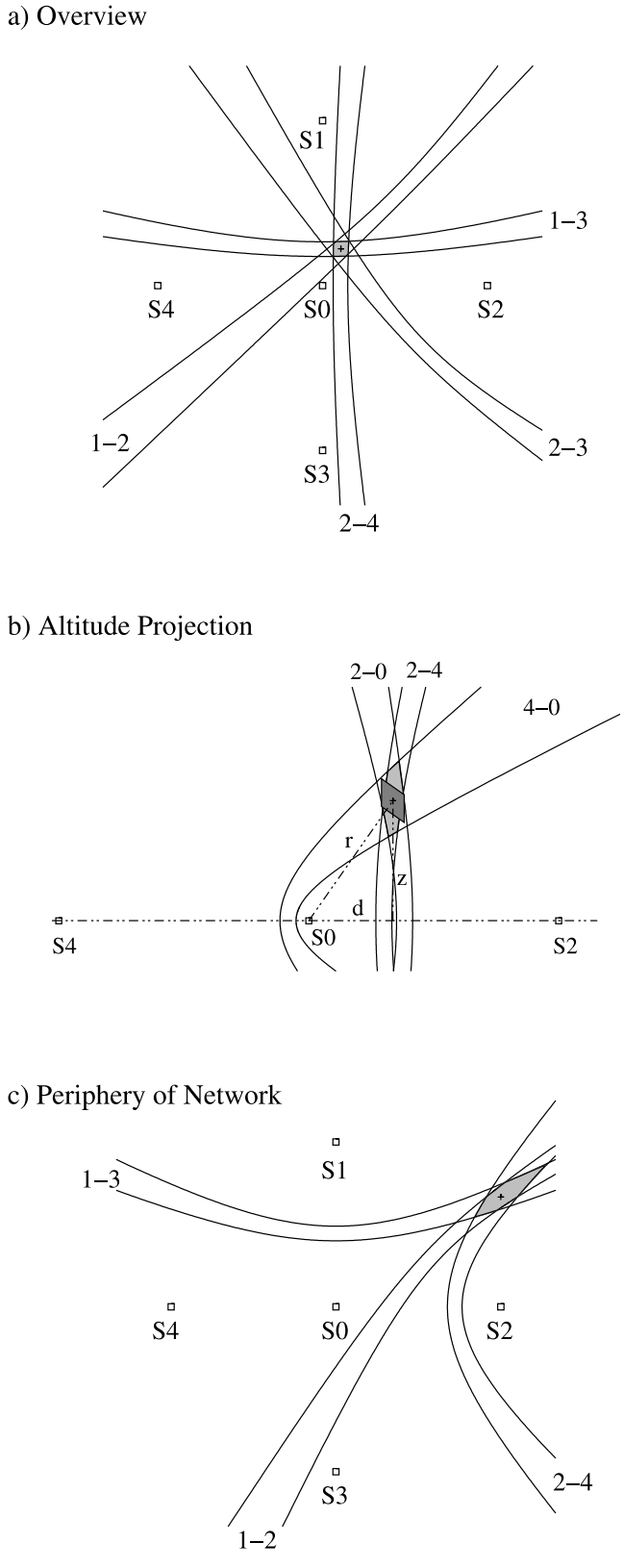

Figure 21. Manner in which the hyperbolae corresponding to arrival time differences at pairs of stations constrain the location and accuracy of sources situated over or near a TOA network. The sets of hyperbolae for the different station pairs indicate the effect of timing uncertainties at those stations on the location. For example, the "2–4" hyperbolae denote the uncertainty in the location from measurements made at stations S2 and S4 (see text). The inscribed parallelogram in Figure 21b is from the simple model of Figure 6b and assumes the same errors used to generate the sets of hyperbolae.

effect of the uncertainty in the TDOA values at the stations. The magnitude of the errors is greatly exaggerated for purposes of illustration. As can be seen, when the source has stations in different directions, its location is constrained to be in an enclosed region that is approximately circular. This is the fundamental basis of the horizontal error model in Figure 6a for sources over the network. Hyperbolae are shown only for pairs of outlying stations (S1–S4) and not for the central station.

[80] Figure 21b illustrates how the hyperbolae associated with the close station (S0) defines the altitude of the source, in comparison with the simple geometric model of Figure 6b. Three sets of hyperbolae are shown, corresponding to the time differences of the "inner" station pairs (2–0 and 4–0) and the "outer" station pair (2–4). Examination of the hyperbolae shows that height is most constrained by the inner pair off to the side of the source, i.e., by the 4–0 pair. The 2–0 and 2–4 differences primarily restrict the horizontal position because the stations are on both side of the source. The inscribed parallelogram is the simple model result corresponding to the same timing errors; it provides a good estimate of the horizontal uncertainty (even though the source is well above the plane of the network) and slightly underestimates the height uncertainty.

[81] Figure 21c shows how the uncertainty of the plan location increases for a source just outside the periphery of the network. The uncertainty has become primarily radial relative to azimuthal uncertainty. The source still has stations in opposite directions in the azimuthal direction but not in the radial direction. The radial error was the primary cause of the increased E–W and N–S errors seen during the balloon flight as the balloon drifted outside the network (Figure 5).

[82] Figure 22 shows the hyperbolic geometries for locating a source outside the network. As in the model formulations of Figure 11 the source is assumed to be east of the network to illustrate the effect of the transverse and longitudinal stations in determining the location. The plan view of Figure 22a shows how the hyperbolae associated with the transverse stations (S0, S1, S3) locate the source azimuth and range. The combination of the inner arrival time differences 3–0 and 1–0 determine the range of the source, consistent with the model idea that these time differences determine the curvature of the wavefront. While the same time differences also constrain the source in the azimuthal direction, the greatest constraint is provided by the outermost stations, 3–1, as in the model. Also, the range uncertainty has become relatively larger than the azimuthal uncertainty. Note that the projection can be in any plane passing through the transverse stations and thus gives the three-dimensional radius or "slant range" to the source.

[83] The vertical projection of Figure 22b illustrates how the longitudinal stations determine the elevation angle of the source. The elevation angle, in combination with the range from the transverse stations, determines the height of the source. The most distant station pair, 4–0, least restricts the elevation angle. Both the close inner pair (2–0) and the outer pair (2–4) restrict the elevation angle by about similar amounts, with the outer pair being somewhat better owing to the larger distance between the stations. (The 2–4 pair would become increasingly better for more distant sources.) None of the longitudinal station pairs serve to constrain the range of the source, which is determined by the transverse stations. In the example shown the altitude uncertainty is mostly due to the range error and to a lesser degree to the elevation angle error. However, for more distant sources at the same altitude the elevation uncertainty would dominate the height uncertainty, again as indicated by the model.

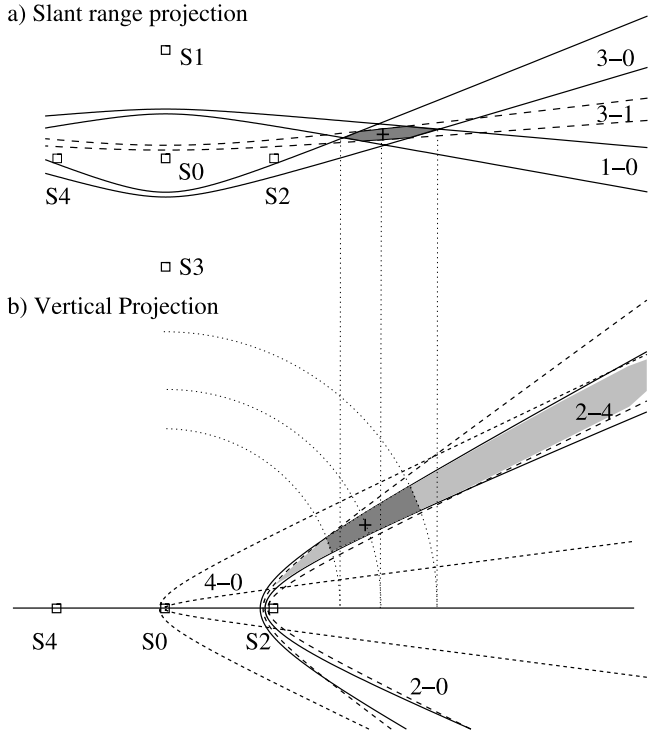

Figure 22. Same as Figure 21, but for sources outside the network. (a) The top projection shows how the transverse stations (S1, S0, S3) determine the range and azimuthal position of the source and apply in the slanted plane passing through the through the transverse stations and the source. (b) The vertical projection shows how the longitudinal stations (S2, S0, S4) determine the elevation direction of the source which, in conjunction with the range, gives the source altitude (see text). The dotted lines provide a geometrical construction for incorporating the slant range information into the determination of the source height.

[84] In summary, the results of the simple geometric models are fully consistent with those of the more rigorous hyperbolic formulations. The advantage of the geometric models is that they provide first-order analytical estimates of the location uncertainties.

7. Summary and Further Discussion

[85] Time of arrival systems such as the Lightning Mapping Array constitute a highly accurate and discriminatory space-time correlation filter. Noise signals that do not arrive "at the right place at the right time" are mostly excluded from solutions, whereas signals emanating from a common source can be accurately located. The basic unit of location accuracy is $c\Delta t$, where Δt is the rms uncertainty in the TOA measurements at each location. The value of Δt is best determined from the distribution of goodness of fit values (Figures 9 and 10). For the STEPS network, Δt was

determined to be 43 ns rms for deterministic pulses from a balloon-borne transmitter and about 50 ns rms for typical lightning observations. These are overall values that include the effect of the various different sources of error or uncertainty, including small systematic timing and positional errors, and are representative of the performance of the STEPS network. For 50 ns errors, $c\Delta t = 15$ m; the location uncertainties are proportional to $c\Delta t$ and scale upward or downward depending on the source location relative to the network and the direction in which the uncertainty is being evaluated.

[86] With the above accuracy, impulsive events over the central part of the network are located with an uncertainty as small as 6–12 m rms in the horizontal and 20–30 m rms in the vertical. The uncertainty gradually increases with distance away from the central part of the network. For sources outside the network the range and altitude uncertainties increase as the square of the range, r^2, while the azimuthal uncertainty increases linearly with r. The difference in the r dependence causes the range uncertainty to dominate over the azimuthal uncertainty so that plan views of distant storms are radially elongated. For large-diameter networks such as the one used during STEPS ($D \simeq 70$ km) the range and altitude uncertainties are comparable to each other for sources at typical lightning altitudes ($z \simeq 5$–10 km). For smaller diameter networks the range uncertainty exceeds the altitude uncertainty, for example, by about a factor of 5 for the 16-km-diameter LDAR network.

[87] The location accuracy outside the network also depends on the network diameter and is conveniently expressed in terms of the rms uncertainties at 100 km range. For the 70 km diameter network operated during STEPS the range uncertainty at 100 km range was found experimentally from aircraft tracks to be 300–600 m rms. The altitude uncertainty was comparable in magnitude. The measured errors were somewhat larger than the optimal uncertainties, which from covariance error analyses were $\simeq$200–300 m rms for range and altitude, assuming all stations participated in the solutions. The uncertainty in azimuthal position was an order of magnitude smaller, being 20–30 m rms for all-station solutions.

[88] The difference between the observed and optimal errors is that all stations usually do not participate in solutions. Spark-type discharges such as those produced by lightning or aircraft are most often located by the minimum allowed number of stations, which is $N = 6$ for the LMA processing (Figure 10). One reason for this is that the radiated source powers P of natural lightning have an approximate $1/P$ distribution [*Thomas et al.*, 2001] so that most located sources are low-power events that will tend to be detected by a minimal number of stations (often but not necessarily the closest stations). A typical LMA network has 10–12 measurement stations; the larger number of stations increases the likelihood that events will be located by more than the minimum number. Empirically, however, the primary advantage of increasing the number of stations is that more sources are located during a given lightning discharge.

[89] The effective timing uncertainty as determined from the distribution of goodness of fit values varies somewhat with the number of stations participating in the solutions and also from one data set to another. These effects are the subject of continued study; they can be caused, for example, by different stations being operational on a given day or during a given storm, by temporal variations in the background noise levels at the stations, differences in storm location, and possibly even by differences in the nature of the lightning activity itself. For the STEPS observations the effective rms timing uncertainty Δt has been found to vary from 43 to 55 ns for lightning solutions involving seven or more stations. The most recent LMA network, the University of Oklahoma/National Severe Storms Laboratory system in central Oklahoma, has smaller effective timing uncertainties, ranging from 38 to 45 ns rms for lightning sources located at six or more stations. The improvement likely results from the use of newer and more identical stations and electronics configurations and more accurate determinations of the positions and time delay values for the individual stations.

[90] As discussed in Appendix A, locally generated noise is always present in the data from each station. Local noise events impact the observations and the location uncertainties in several ways. First, the noise limits the station sensitivity by increasing the level above which lightning events can be detected. If a local noise event is stronger than the lightning event to be located and occurs within the same measurement time window, it prevents that station from participating in the solution for the lightning source. By chance, a small fraction of local noise events happen to lie close enough in time to the lightning event and are incorporated into the set of arrival times used to locate its source. In the latter case the data are "contaminated," and the source location is in error by some amount. Some of the contaminated source locations are obviously in error, but the contamination is not always obvious, nor can contaminated sources be identified objectively on the basis of residuals or goodness of fit values.

[91] The balloon sounding data indicate that noise-contaminated solutions typically comprise <1% of the located sources. Obviously contaminated locations can be substantially reduced or eliminated by restricting the sources to those located by $N = 7$ stations or more. This eliminates a significant number of valid solutions but can be useful when looking at the overall lightning activity in a storm or in other situations where there are a large number of sources (e.g., Figures 3, 13, and 15). A good compromise for lightning measurements that maximizes the number of valid solutions while keeping contaminated events at an acceptable level is to have the minimum number of participating stations be $N = 6$ and to vary the goodness of fit value below which the data points are utilized for anaylsis. Empirically, for the LMA observations, this occurs for goodness of fit values $\chi^2_\nu \leq 2$ (see section A2).

[92] Other factors that degrade the location accuracy are more difficult to quantify and usually cannot be controlled. For example, if the emitting region is larger than the radio frequency wavelength ($\simeq$5 m), or if the radiated signal is not impulsive, the source may be timed differently at each station. The result will be a poorer fit to the arrival times and a more uncertain location. Similarly, continuous radiation events such as stepped or dart leaders that have weak or multiple embedded impulsive events can give incorrect or noisy locations. Observations of such events are substantially improved by decreasing the width of the measurement time windows. The LMA is typically operated either with 80 or 100 μs time windows or in high-resolution mode with

10 μs time windows. With 10 μs windows the observations are best made with small-diameter networks and can be used for detailed studies of individual lightning discharges [*Rison et al.*, 2000; *Behnke et al.*, 2003]. A compact array of mapping stations is currently being operated in 10 μs mode at New Mexico Tech's Langmuir Laboratory for Atmospheric Research. Eight stations are deployed within a 4 km diameter area, and four outlying stations over a 60 km diameter area, for detailed studies of lightning over the mountaintop laboratory.

[93] The LMA is able to monitor lightning activity over a relatively large geographical area compared to the dimensions of the network itself. Observations during STEPS showed that lightning-producing storms can be monitored out to 200–300 km range, namely over an area 400–600 km (250–375 miles) in diameter. Such monitoring is now routinely conducted by the North Alabama LMA being operated by NASA's National Space Science and Technology Center (NSSTC) [*Goodman*, 2003; *Koshak et al.*, 2004] (http://branch.nsstc.nasa.gov). The NSSTC group processes the data in real time and supplies the resulting "total lightning" observations to the National Weather Service office in Huntsville, who are evaluating its usefulness in nowcasting severe weather [*Darden et al.*, 2003]. Real-time processing and display has recently been developed for an LMA being operated in central Oklahoma by OU/NSSL (see http://lightning.nmt.edu/oklma). A third LMA system is currently being installed for weather monitoring and nowcasting studies at White Sands Missile Range in central New Mexico. Finally, a similar, commercial version of the mapping system, called LDAR-II, is being operated in the Dallas-Fort Worth metropolitan area by Vaisala, Incorporated [*Demetriades et al.*, 2004; L. D. Carey et al., Lightning location relative to storm structure in a leading-line, trailing-stratiform mesoscale convective system, submitted to *Journal of Geophysical Research*, 2004], and a second LDAR-II system is soon to be set up in the Houston, Texas, area as part of the Houston Environmental Aerosol Thunderstorm (HEAT) project planned during 2005.

[94] In addition to making lightning observations, the mapping system is able to detect and track aircraft flying through ice crystal clouds over or near the network. The aircraft emit a steady sequence of sparks as a result of collisional charging with the ice crystals, and the sparks are often strong enough to be located. The source powers of the aircraft sparks are just above the minimum detectable values of the LMA, and the ability to detect such tracks is a good indication of the network sensitivity. Since most located lightning events also have source powers near the minimum value, such lightning events are energetically similar to the aircraft discharges.

[95] The sounding balloon measurements show that airborne instruments or aircraft can be accurately tracked in the vicinity of a network by having the platforms carry a pulsed transmitter whose frequency is in the passband of the mapping system. The transmitter can be compact and lightweight and can operate with a low duty cycle for extended time periods from a small battery. Limited amounts of data can be transmitted to ground by modulating the time between transmitted pulses (Appendix D).

[96] Finally, the TOA mapping technique can be used for other kinds of applications. Examples include the detection and monitoring of faults on power transmission lines, tracking of ground-based equipment or personnel carrying pulsed transmitters, and studies of radio frequency interference from buildings and other installations. A set of lightweight, compact, and readily deployable mapping stations is currently being constructed to be used use both for lightning studies and other applications. The system will be portable and can be operated from automotive batteries and will enable observations to be made in locations and situations where they would otherwise not be feasible.

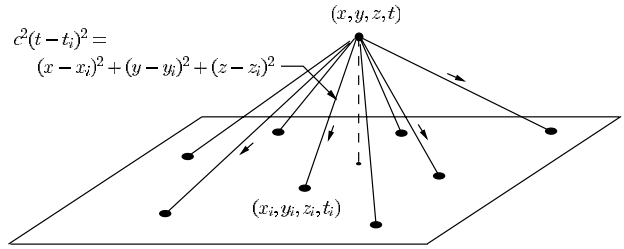

Figure A1. Basic TOA technique. Measurements of the arrival times t_i at $N \geq 4$ locations are used to determine the location and time of the source event (x, y, z, t).

Appendix A: The Lightning Mapping Array

[97] In this appendix we describe the basic way in which the LMA operates and the manner in which its data are processed. Figure A1 shows the basic geometry of the TOA technique. An impulsive radiation event occurring at (x, y, z) and time t is received at a number of measurement locations on the ground. At location (x_i, y_i, z_i) the arrival time is t_i, according to

$$c(t - t_i) = \sqrt{(x - x_i)^2 + (y - y_i)^2 + (z - z_i)^2}), \qquad \text{(A1)}$$

where c is the propagation speed of the signals. Measurements of t_i at $N \geq 4$ locations can be used to determine the four unknowns (x, y, z, t). The mapping network deployed during STEPS consisted of 13 stations spread over a 60 × 80 km area in northwestern Kansas and eastern Colorado (Figures 3, 13, and 15). Other LMA networks in Alabama and Oklahoma consist of 10–12 stations spread over similar or slightly smaller areas. The stations are spaced typically 15–20 km apart and are connected by wireless communication links into a central location. The communications enable the station operation to be monitored and controlled and also enable real-time processing and display of the data.

[98] Each LMA station receives the lightning signals in a locally unused television channel in the lower VHF band (usually TV channel 3, 60–66 MHz). The radio signals are logarithmically received over a large (80 dB) dynamic range, and the detected signals are digitized using a specially designed data acquisition and processing card (the LMA card) interfaced to a standard PC. The LMA card digitizes the signals at a 25 MHz rate and determines the arrival times of the peak events in successive 80 μs time intervals, or "windows." (The initial version of the LMA cards digitized the receiver output at a 20 MHz rate and had 100 μs time windows. The STEPS network consisted of both types of stations.) Events are captured only when their

peak amplitude exceeds a threshold value which can be remotely or automatically adjusted at each station. Typical threshold values correspond to received power levels of −70 to −80 dBm at the antenna output, depending on local site noise. Sites have to be specially tested and selected to provide this level of sensitivity and are usually situated in remote locations. Typical threshold values enable the array to detect radiated source powers down to a few tenths of a watt in the receiver passband for events over or near the network (Figure 17).

[99] The above operation enables each station to detect up to 12,500 events, or "triggers," per second, corresponding to the number of 80 μs intervals in 1 s (10,000 events s^{-1} for systems having 100 μs windows). The threshold values are typically adjusted to produce ≃100–1000 triggers s^{-1} in the absence of lightning. The background trigger rate is caused by local corona and radio frequency interference at each station, which varies with time, sometimes substantially and even over relatively short (second) time intervals. Anomalous propagation or variable reception of distant television stations in the receiving channel can also interfere with the operation of the network. The composite video of an interfering television signal will trigger the system at the full rate so that the threshold needs to be adjusted to be above the peak of any interfering television signal level.

[100] The data stream from the LMA card is assembled into a sequence of 10 Mb or larger files and recorded locally on disk. Decimated data are communicated to a central location for real-time processing and display. The decimation typically selects the strongest radiation event in five successive windows, namely in a 400 μs time window. The data stream includes the arrival time of the peak event (with the 40 ns time resolution of the digitization) as well as the peak signal amplitude (with 0.5 dB resolution). A header is placed in the data stream at the beginning of each second, which contains time information for the current second and related diagnostic information.

[101] The overall data rate is 73 kb s^{-1} when the system is triggering at full rate and 4–8 kb s^{-1} for 5–10% trigger rates. At the latter rates and depending on storm activity a 40 Gb disk can record the data at each station for up to 60–120 days. The decimated data rates are proportionally lower and can be communicated over the wireless links for real-time processing. In current systems the primary data recording is on hard disk at each station, with the disks being swapped out as they become full and their data transferred to RAID drives for postprocessing as desired. Diskless operation is possible when fast communication links are available into a central location.

[102] The stations can also be operated in high-rate mode. This mode, used for detailed lightning studies, determines the peak radiation event in successive 10 μs windows and can be initiated remotely by uploading different firmware into the LMA card.

A1. Timing Considerations

[103] A fundamental difference between the LMA and the current and early LDAR systems at Kennedy Space Center is that the TOA values are measured independently at each station rather than at a central site. The independent timing was made possible by the availability of inexpensive, compact GPS receivers capable of providing an accurate time base at each station. It has the substantial advantage of significantly reducing the data rate needed to communicate the measurements to a central location for real-time processing. In turn, this allows the communications links to be digital for increased reliability and noise immunity. The independent timing also enables the stations to be operated independently of each other, without communications links, allowing a network to be deployed and operated in situations where measurements would otherwise not be possible. The GPS receivers at each station output a 1 pulse s^{-1} signal whose timing is accurate to a few tens of nanoseconds rms. The signal is used to control the frequency of a master 25 MHz oscillator on the LMA card. The oscillator frequency is controlled within a few counts per second of an exact 25 MHz rate, and the difference from the exact count is recorded in the data stream and used to compensate the arrival times during the data processing.

[104] The fact that the arrival times are quantized in 40 ns increments causes a random timing error, whose rms value is $40/\sqrt{12} \simeq 12$ ns [e.g., *De Fatta et al.*, 1988]. The quantization error adds in quadrature to the other errors and contributes in a minor way to the overall timing uncertainty of ≃50 ns rms. A related error arises from the fact that the receiver output is quantized in amplitude as well, introducing an additional uncertainty in the time of the signal peak. The effect of the amplitude quantization is reduced by using 12 bit bipolar (11 bit unipolar) digitization rather than the 8 bit digitization available for the earlier LDAR system. Short-duration radiation events impulsively excite the receiver, causing its output to oscillate, or "ring," with the impulse response of the receiver bandpass. The 3 dB width of the ringing amplitude is approximately $1/B \simeq$ 170 ns, where $B = 6$ MHz is the filter bandwidth. At the 0.06 dB level corresponding to the 11 bit digitization the response width is about 22 ns. This somewhat increases 40 ns quantization of the temporal sampling.

[105] The deterministic pulses of the sounding balloon measurements are indicative of the magnitude of the system-related errors. The pulses were 125 ns in duration, corresponding to ≃8 cycles of 63 MHz radiation. The finite duration of the pulses somewhat broadens the width of the receiver response relative to impulsive inputs, and the overall timing errors for the pulses were about 43 ns rms (Figure 9). Except for the broadening, the 43 ns value represented the combined effects of clock uncertainties associated with the independent timing measurements, signal quantization, and receiver signal-to-noise effects, which cause weak signals to be timed less accurately than strong signals. It also includes additional uncertainties such as those associated with the exact position of the receiving antenna and the time delay from the antenna into the LMA card. The peak power of the balloon transmitter was relatively low, on the order a few watts, but with a duty cycle of about 10^{-5}, resulting in the average power being minimal. In some respects, the transmitter pulses are similar to lightning signals, most of which have low power levels in the receiver passband and are often broadened as well.

[106] The rms timing errors of lightning signals for the STEPS observations were somewhat larger, ≃50 ns rms, but not substantially larger. The increase in the timing error indicates that the lightning signals themselves introduced an additional uncertainty of about $\sqrt{50^2 - 43^2} = 25$ ns to the

measurements. This represents the effects of the nondeterministic nature of the lightning signals, such as not being impulsive in time and/or localized in space.

A2. Solution Technique

[107] The data processing solves the TOA equation (A1) to determine the source location and time from the measured arrival times. For the LMA data, this is done on a second-by-second basis using the nonlinear least squares Marquardt algorithm. The algorithm minimizes the chi-square goodness of fit value

$$\chi^2 = \sum_{i=1}^{N} \frac{\left(t_i^{\text{obs}} - t_i^{\text{fit}}\right)^2}{\Delta t_{\text{rms}}^2}, \tag{A2}$$

where t_i^{obs} is the measured arrival time at the ith station, t_i^{fit} is the predicted arrival time from equation (A1) for each trial solution, and N is the number of stations participating in the solution. Δt_{rms} is the uncertainty of the timing measurements, assumed to be a constant and the same for all stations. The Marquardt algorithm minimizes χ^2 in an iterative manner by linearizing the TOA equations for each station around successive trial solutions and by solving the linearized equations to obtain the next trial solution. As discussed by *Bevington* [1969], the linearized curvature matrix used to obtain the solution can be inverted to obtain the covariance matrix describing the uncertainties of the (x, y, z, t) values [see also *Koshak et al.*, 2004]. Finally, because the value of the timing uncertainty Δt_{rms} is not necessarily known a priori, a nominal value of 70 ns is assumed in the processing. The resulting χ^2 values are readily scaled to any constant rms error, however, by multiplying by $(70\text{ ns}/\Delta t_{\text{actual}})^2$.

[108] The goodness of fit values are normalized relative to the number of measurements N by determining the reduced chi-square value, $\chi_\nu^2 = \chi^2/\nu$, where $\nu = (N - 4)$ is the number of degrees of freedom (i.e., the number of redundant measurements) for the solution. The χ_ν^2 values have a known statistical distribution when the measurement errors are Gaussian distributed, which depends only on ν. As discussed in section 3.1, the distribution of measured χ_ν^2 values for different degrees of freedom provides the most accurate way of estimating the overall errors of the system.

[109] In processing the LMA data, we require that a minimum of $N = 6$ stations participate in a solution, providing two or more redundant measurements as a check on the solution's validity. Most lightning sources are located by the minimum number of stations, whereas the deterministic pulses from the balloon-borne transmitter were most often located by measurements at 10 stations. The fact that there is good agreement between the observed and theoretical distribution of χ_ν^2 values indicates that most of the measurement errors are Gaussian distributed. The nonzero tail seen in the distributions for the lightning sources in Figure 10 is indicative of an additional, uniform error contribution, presumably due to the lightning events being nonimpulsive.

[110] From the statistical distribution of goodness of fit values in the presence of Gaussian errors (e.g., Figures 9 and 10) the restriction $\chi_\nu^2 \leq 2$ passes about 90% of valid data points. This applies to actual chi-square values, namely those adjusted to take into account the difference between the actual and assumed rms timing errors, as described in connection with equation (A2). Thus for 50 ns actual errors an actual chi-square value of 2 corresponds to an unadjusted value of $2/(70/50)^2 \simeq 1.0$. While this restriction is often used in displaying and analyzing lightning observations, the processing typically accepts solutions having larger unadjusted values so as to not miss energetic radiation events.

[111] The solution calculations are performed in a Cartesian coordinate system tangent to the reference surface of the Earth at the coordinate origin for the network. The GPS-derived latitude, longitude, and altitude of the station locations are converted into the Cartesian frame using the WGS-84 ellipsoidal model for the Earth's surface (i.e., the same model used by the GPS), and the (x, y, z) source locations are converted back to geocentric coordinates and GPS altitude in the final output. GPS altitude differs from mean sea level by on the order of 10 m, depending on location. As noted by *Koshak et al.* [2004], the solutions can be obtained directly in geocentric coordinates, but the form of the TOA equation (A1) makes it convenient to work in a Cartesian system.

[112] One advantage of working in a Cartesian frame is that equation (A1) can be cast as a set of linear equations in (x, y, z, t), which are useful in obtaining the solutions. This is done by squaring both sides of equation (A1) and subtracting the equations for $N \geq 5$ stations from each other to obtain $(N - 1)$ difference equations [*Koshak and Solakiewicz*, 1996; *Koshak et al.*, 2004]. In the process the quadratic terms in (x, y, z, t) cancel, leaving only terms linear in the unknowns. In particular, differencing the equations for stations i and j gives

$$x_{ij}\,x + y_{ij}\,y + z_{ij}\,z - c^2 t_{ij}\,t = k_{ij}, \tag{A3}$$

where $x_{ij} = (x_i - x_j)$, etc., $k_{ij} = (1/2)[(r_i^2 - r_j^2) - c^2(t_i^2 - t_j^2)]$, and $r_i^2 = x_i^2 + y_i^2 + z_i^2$. Equation (A3) defines a plane in four-dimensional (x, y, z, t) hyperspace, and the solution is the intersection of four or more such hyperplanes. The arrival time values are incorporated in both the t_{ij} and k_{ij} terms. The advantage of the hyperplane approach is that the equations can be solved analytically for any set of five or more measurements to obtain (x, y, z, t). The disadvantage is that z is poorly determined for networks that are close to planar but not quite planar. The x, y, t values are adversely affected as well. Since actual networks are nearly but not quite planar, the hyperplane approach gives an approximate solution that can be used as the starting estimate for a more accurate least squares solution.

[113] To understand why the hyperplane approach does not give accurate solutions for near-planar arrays, it is helpful first to consider the hyperbolic approach to solving equation (A1). The hyperbolic approach differences equation (A1) for $N \geq 4$ stations directly, without first squaring each equation. This eliminates t as a variable in the equations, giving three or more equations in (x, y, z) only. The equations depend only on the time differences of arrival (TDOA) rather than on the individual arrival times themselves. As discussed by *Proctor* [1971], measurements of the TDOA for a given pair of stations define a hyperboloid

of revolution about the baseline between the stations. The source must lie on the hyperboloid. The solution for (x, y, z) corresponds to the intersection of the hyperboloids from three or more baselines, and the solution for t is then obtained from one or more of the original equations. Although the hyperbolic approach is conceptually useful in understanding the solution (e.g., Figures 21 and 22), the formulations are complex and analytically intractable for all but a few ideal network configurations.

[114] The differencing used in the hyperplane formulations does not eliminate t as a variable, only the quadratic terms in (x, y, z, t). Consequently, a minimum of five measurements are needed to obtain four difference equations to determine the unknowns, in effect discarding one redundant measurement in the process. For the special case in which the network is exactly planar (in the x-y plane, for example), z is eliminated as a variable due to the $z_{ij} = z_i - z_j$ coefficients being identically zero. This would allow the equations for only four stations to be differenced to determine (x, y, t). The height z would then be determined from one or more of the original equations. An analytic, linear least squares version of this approach was proposed by *Koshak and Solakiewicz* [1996] as a means of obtaining solutions for planar networks, instead of the iterative least squares approach.

[115] When the network is not quite planar, the arrival times at the stations are altered from what they would be for a planar network, and one must retain the terms in z in the hyperplane equations. However, the z_{ij} coefficients tend to be relatively small, causing the determinant of the coefficients to be somewhat ill conditioned. The z value is particularly not well determined, and the (x, y, t) values are affected as well. Thus the linear hyperplane approach by itself gives only an approximate solution, as found by *Koshak et al.* [2004]. The hyperplane solution is highly useful as a starting point for the nonlinear least squares procedure, however, and the LMA processing takes advantage of this.

[116] A major issue in processing actual observations is identifying sets of arrival times that correspond to each other and discriminating against events that do not so correspond. This presents a computational challenge requiring that all possible combinations of arrival times be examined to determine which values correspond to common events. The amount of processing needed to do this is substantially increased by the presence of local noise in the data from each station, which cannot be identified as such in advance and which have to be treated as potentially locatable events. The number of events that have to be examined is determined from the physical constraints imposed by the transit time between individual pairs of stations and by the requirement that a minimum of six measurements be available for solutions.

[117] The LMA processing is done in 1 s segments and begins by combining the arrival times at all stations into a single one-dimensional array sorted sequentially by time. (Among other things, this allows data to be combined from stations having different measurement time windows, as, for example, in the STEPS network.) The array contains the arrival times in increasing time order but not in any particular station order, which is identified in a parallel array. The sequential sorting scheme greatly simplifies the search procedure for valid data combinations; by starting at the beginning and going point by point through the array, it is necessary only to look forward from a given data point for candidate sets of arrival times and still explore all possible combinations. The basic assumption is that each arrival time value is the initial event of a locatable source; if it isn't the initial event, it should have been included in an earlier solution, or it is a noise event. The assumption is tested by searching forward in time for six station combinations of data values that satisfy the transit time constraints. The first five arrival times of each such combination would be from stations closest in space to the possible event and are used to obtain the hyperplane solution. To guard against height errors in the hyperplane solutions, physically unreasonable z values are replaced by a nominal, physically reasonable value. In turn, the hyperplane solution is used to predict the approximate arrival times at the other stations, and it is determined if events were detected at the other stations near the predicted times. If six or more stations have possible data, the values are analyzed with the iterative least squares algorithm to obtain a trial solution. This procedure is repeated for all possible six station combinations having the same initial point; the trial solution having the lowest reduced chi-square value (below a specified maximum value) and smallest location uncertainty (from the trace of the covariance matrix) is considered to be the valid result. The metric used is the product of χ^2_ν and the trace. (If χ^2_ν is less than unity, it is assumed to be unity for the purposes of computing the metric.) The data values that participated in the solution are flagged to delete them from further consideration, and the procedure continues to sequence through the array one data value at a time.

[118] A useful option in the processing procedure is to generate a "template" of arrival time differences whenever a valid solution is found. The template is used to search through the full array of arrival times for additional events emanating from sources close to the template solution. Also, two or more combination search passes can be made through the array, first with a low χ^2_ν cutoff value (e.g., 2 or 5), and then with a higher value (e.g., $\chi^2_\nu = 500$). The latter is useful for capturing energetic lightning events that have large χ^2_ν values owing to the source being spatially or temporally extensive.

[119] The overall number of combinations that need to be tested increases rapidly with the total number of stations and with the trigger rates at each station, and this can substantially slow the processing. For the situation in which all stations of a 13 station, 70 km diameter network are triggering at the maximum rate, on the order of 400,000 six station combinations need to be examined by the forward search procedure per starting event. (It was not unusual for full trigger rates to be produced by severe storms during STEPS.) At lesser trigger rates the number of combinations is substantially reduced, and many combinations can be eliminated immediately by the transit time constraints. With current processor speeds and memory capacity, active storms can be processed at rates ranging from faster than real time to factors of 20–50 slower than real time, depending on the number of stations, trigger rates, and the amount of lightning activity. Data decimated to 400 μs sampling windows can be processed faster than real time, even at full data rates. In highly active storm situa-

tions, it is not unusual for more than a million sources to be located in a 10 min time interval.

[120] In principle, the received power values at each station could also be used to help identify potential sets of data points (or even, in the least squares minimization, used to locate the source) since the power values will tend to decrease with distance from the source. In practice, however, the received power values from sources differ substantially from the expected $1/r^2$ range decrease due to local receiving effects at each station (interference, attenuation) and to the unknown radiation pattern of the lightning source itself. The measured signal powers are therefore used only after the source location is determined to estimate the source power.

Appendix B: Systematic Errors

[121] In this appendix we address the issue of systematic errors and their effect on the location results. The TOA technique basically solves the equation velocity × time = distance, or $vt = d$. More specifically, it solves $v\Delta t = \Delta d$, where Δd and Δt are the differences between the source and station locations and arrival times. The quantity v is the propagation speed. Systematic errors can arise from inaccurate values of any of the three quantities v, Δt, or Δd. So far, we have considered all errors to be lumped into an effective timing error; that is, the errors are considered to be "time-like." However, the effective timing error can include contributions from imprecise station positions or propagation speeds. Positional errors would be important if they are comparable to the overall 40–50 ns timing uncertainty of the system, namely 12–15 m (40–50 ft).

B1. Timing Errors

[122] Because the clocks used for measuring the arrival times operate independently at each station, systematic errors can be present in the timing data. These errors are due to the digitizer clock frequencies being slightly different at the individual stations and would be cumulative with time. Indeed, such errors are seen in both the airplane and balloon track observations. Figure B1 shows an expanded view of 17 km of the 25 June airplane track. In the plan view the scatter of the sources is in the SW-NE direction, i.e., radially away from the center of the network to the southwest. The source locations exhibit a characteristic sawtooth pattern in which the mean range steadily increased and then suddenly decreased, often by 200–300 m or more.

[123] The large decrease, or "jump," near the center of the track in Figure B1 was slightly greater than 500 m in range. This and the other range jumps were accompanied by changes in the apparent height of the sources; for example, an 800 m height decrease occurred at the time of the 500 m range jump. The jumps occurred at intervals of 1.5–2 km along the track, corresponding to time intervals of 6–8 s. Also, when plotted versus time instead of position, the jumps occurred precisely at 1 s boundaries. A similar sawtooth pattern was seen in the 25 May airplane track, but the jumps were smaller (on the order of 100 m) and increased rather than decreased the range. The 25 May jumps were spaced about 1 km apart, corresponding to about 4 s time intervals, and also occurred at second boundaries. Similar sawtooth-type variations are also seen in the expanded balloon sounding data (Figure 4).

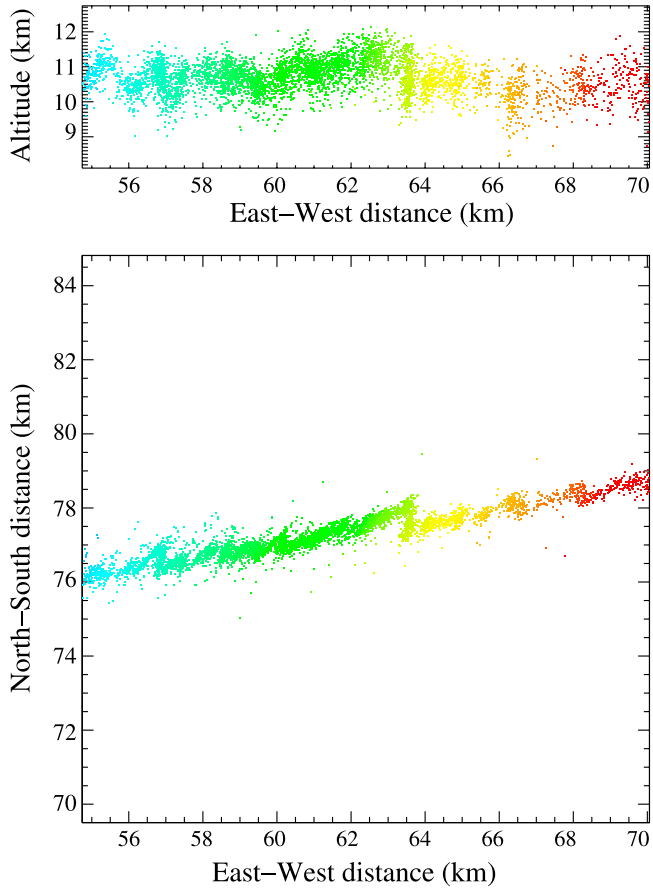

Figure B1. Expanded view of the 25 June aircraft track, showing (bottom) the sawtooth pattern of source locations caused by accumulated timing errors in the plan view and (top) similar systematic height variations. The sudden decreases or jumps in the locations occur at 1 s boundaries, which is when cumulative timing errors are reset in the GPS output at individual stations (see text).

[124] The sawtooth pattern of source locations indicates a gradual buildup of systematic errors in the TOA values, followed by a sudden correction of the errors. The size of the jumps is comparable to the random scatter, indicating that the systematic errors are comparable in magnitude to the random errors. The fact that the jumps occur at second boundaries indicates they are due to corrections in the timing of the 1 pulse-per-second (pps) output from the GPS receivers at the stations.

[125] As described in Appendix A, the 1 pps output is used to control the frequency of a 25 MHz oscillator on the LMA card. More importantly, however, the 1 pps transition provides the starting point for the timing measurements for each ensuing second. The GPS receivers have their own internal 10 MHz clock, which is free-running, and the 1 pps transitions are synchronous with the 10 MHz internal clock transitions. The time of the 1 pps transition occasionally slips by one cycle of the internal oscillator, or by 100 ns, as needed to stay in synchronization with actual time. The correction occurs independently at the different stations and evidently causes noticeable corrections in source locations every few seconds or so. The ramps between corrections are

caused by the 25 MHz clocks at each station not being precisely adjusted. This results in the gradual accumulation of small timing errors during each second. The data stream contains information used to compensate for this effect in the processing, but residual effects remain.

[126] The magnitude of the time corrections can be estimated from the size of the jumps and from the model formulations of section 4. The 500 m range decrease in Figure B1 occurred at a distance close to r = 100 km and therefore corresponded to a fractional change of −0.005 in range. In the context of the simple model the range is determined by the difference $T_{13,0}$ in the arrival time at the outer transverse stations relative to the central station (Figure 11c). From equation (4), $T_{13,0}$ = 20 μs for a storm at 100 km range. Also, a −0.005 fractional range change would have corresponded to a +0.005 fractional change in $T_{13,0}$. The sudden jump in $T_{13,0}$ would thus have been +0.005 × 20 μs, or 100 ns. This is the value that would be expected from the 1 pps signal slipping by one 10 MHz clock cycle. Either a single station was primarily responsible for determining the range, or the timing was fortuitously corrected at the same second at two or more stations that were determining the range. The fact that most jumps were smaller than 500 m indicates that the timing corrections were at stations that had less influence on the range value.

[127] The sawtooth variations make a significant contribution to the rms scatter about the aircraft tracks, comparable to the random errors. Both the systematic and random errors are accounted for in the overall timing uncertainties, however, and therefore in the covariance- and model-predicted location uncertainties as well. GPS receivers currently provide additional information on the offset of the 1 pps transition from true time; use of this information should enable the sawtooth errors to be reduced below detectable levels in future versions of the LMA.

[128] Systematic timing errors also arise if the time delays between the VHF antennas and the digitizer at each station are imprecisely known. The delays are on the order of several hundred ns and differ from station to station due to different cable lengths and any differences in the receiver components. Examination of the residuals of data solutions at each station provides a way of detecting and correcting large (≃40 ns) systematic errors, but usually not smaller errors.

B2. Spatial Errors

[129] Systematic spatial errors can result from imprecise values of the station locations. The station positions are determined by averaging the output of each station's GPS receiver for a few hours to a day or more. Tests indicate that a few-hour average determines the GPS antenna position to within about 1–3 m in the horizontal and 2–7 m in the vertical. These results are obtained in the absence of selective availability (the purposeful introduction of errors into the GPS transmissions), which was turned off on 2 May 2000, just prior to the STEPS field observations. The location information required in the processing are the positions of the VHF antenna at each station, which is typically located 30 m or so away from the station electronics and GPS receiver. (This is done to reduce radio frequency interference from the electronics below detectable levels at the antenna. In some networks and sites, it is also needed for the VHF antenna to be clear of local obstructions.) With some care, the x, y, z offsets between the GPS and VHF antennas can be measured to ≃1 m or so and should not contribute significantly to the overall error.

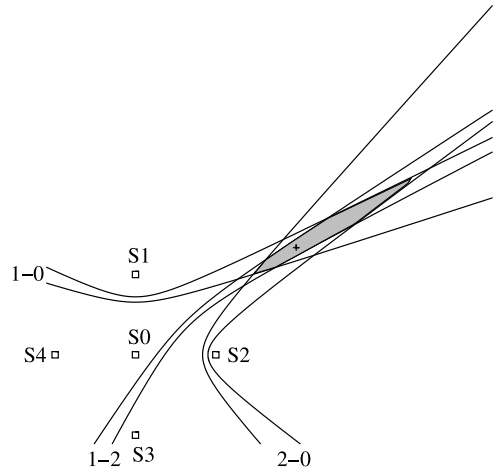

Figure B2. Hyperbolic geometry for the plan location of a distant source, illustrating how measurement errors cause asymmetric location errors and bias the source location outward in range.

[130] Station location errors have the greatest effect on the height of sources in distant storms. The height of distant sources depends on the elevation angle of arrival, θ, and the range r. As discussed in connection with Figure 11d, θ is determined primarily from the arrival times at the close and far stations along the arrival direction. For distant sources, θ is small, and the arrival times differ only by a small amount from the transit time between the stations. Relatively small errors in the presumed station locations (or in the measured TOA values) cause errors in θ whose effect is magnified for distant events. This is illustrated in section B3.

B3. LDAR Height Errors

[131] As discussed in sections 1 and 5.2, B2001 found a systematic increase in the height of the maximum lightning activity with distance from the LDAR network. The maximum lightning activity occurred at 9 km altitude in storms over and close to the network but artificially increased up to 20 km altitude at 300 km range. B2001 explained the height increase as being due to larger than expected range errors and to a consequent tendency for located events at large distances to be dominated by overranged events from intermediate-distance storms. Assuming a constant elevation angle, the overranging increased the apparent altitude of the sources. The range errors appeared to be large from observations of distant storms in the LDAR data, as discussed in section 5.2. In turn, the explanation of the systematic height increase supported the idea of larger than expected range errors.

[132] Figure B2 illustrates how TOA networks will tend to overrange sources outside the network. If the measurement errors are sufficiently small, the location uncertainties are symmetric about the source location. However, if the errors are not sufficiently small (or even for small measurement errors, at sufficiently large range), nonlinear effects cause the uncertainties to be asymmetric and the average

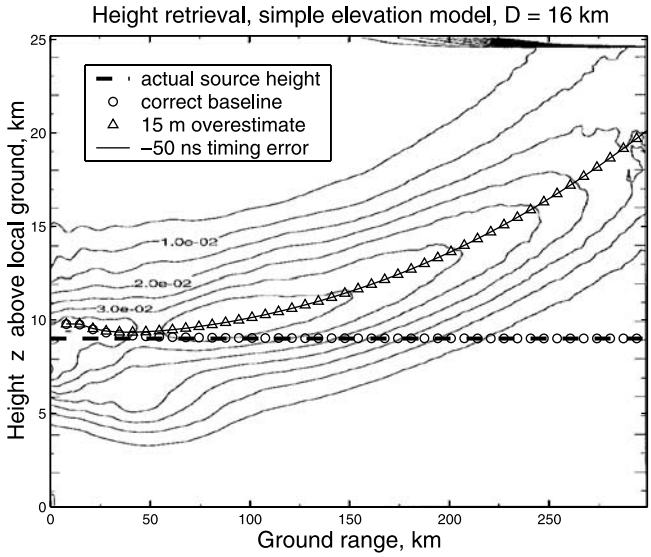

Figure B3. Predicted height increase with range for sources at 9 km altitude if the baseline distances of the 16-km-diameter LDAR network were overestimated by 0.1% (15 m) (triangles) or, equivalently, if the arrival time differences at close and far stations were underestimated by 50 ns (solid curve). The results are overlaid on observations of the systematic height increase found by *Boccippio et al.* [2001] (contours); all heights are above the local Earth (see text).

location to be biased outward in range. The bias occurs even in the absence of systematic measurement errors and can be seen from the hyperbolic geometry of how distant sources are located. The bias is exacerbated when the errors are large, due either to the range itself being large and/or to large errors in the measurements themselves.

[133] B2001 showed that overranging of sources at intermediate distances (due both to random errors and biasing of the range values) provided a possible explanation of the systematic height increase with distance. However, the range errors needed to do this were an order of magnitude larger than those that were expected from aircraft measurements. They were also larger than would be expected from the size of the LDAR network and its timing errors (section 5.3). B2001 assumed that elevation errors were not a significant factor in the height increase, but this was an incorrect assumption which, when taken into account, provides a simple and better explanation of the systematic height increase.

[134] Figure B3 shows the effect of a systematic baseline or timing error on the apparent height of sources versus range from the LDAR network. The results are overlaid on the source density contours from Figure 7 of B2001. The comparison shows that the observed height increase is perfectly fitted if the baselines between opposite sides of the network were systematically overestimated by 15 m (triangles). Equivalently, the time differences of arrival at opposite sides of the network were systematically underestimated by 50 ns. The height values were determined using the model result equation (6) for the elevation angle of distant sources in the presence of the systematic errors. When correct baseline and timing values are used, the model slightly overestimates the 9 km height of sources within 30–50 km range of the network but accurately estimates the source heights at larger ranges (circles). The calculations assume that the effect of the range error upon the source height was small compared to the elevation error, as shown in section 4. Biased and random range errors would still have an effect, but this will be small in comparison to the elevation errors. Whatever the range errors of the LDAR system may have been at large distances, the uncertainty in the elevation angle is the dominant factor in the source height values, and overly large range errors are not necessary to explain the systematic height increase.

[135] It is not possible to determine the detailed cause of the height error without knowing the specifics of the LDAR operation and processing. However, the above results indicate that it was due to a systematic baseline or timing error. A 15 m baseline overestimate corresponds to a 0.1% fractional error in the 16 km baseline length D. Systematic baseline errors will occur if imprecise values are used for the local radius of curvature of the Earth, namely if the WGS-84 model is not used to convert station latitude and longitude values to Cartesian coordinates in the data processing. The mean radius of the Earth is 6370 km but varies from 6378 km at the equator to 6357 km at the poles. A 0.1% or 6.4 km overestimate of the assumed radii of curvature would give the observed results. Systematic height errors in distant storms have been obtained in the LMA processing, both from not using the WGS-84 conversion and by processing data with purposely incorrect station locations. The accuracy of the TOA technique is such that the results are sensitive to the shape of the Earth.

[136] Alternatively, from equation (6), the same systematic height error would be produced if the arrival time differences $T_{4,2}$ at the close and far stations were underestimated by 0.1% (or if the propagation speed was underestimated by the same amount). For a 16 km baseline, $T_{4,2} \simeq 53.3$ μs for distant sources. Systematically underestimating the arrival time differences by about 50 ns therefore would give the same height errors, as indicated in Figure B3. Such a systematic timing error would tend to average to zero in the azimuthally integrated data of B2001, but land-sea asymmetries in the amount of lightning activity around the LDAR network could allow a bias not to average to zero. (Systematic timing errors of 50 ns should also be detected in the pulser data used to calibrate and monitor the LDAR's operation.) From the subsequent discussion on propagation speeds, absent an artificial error, it would be difficult to underestimate the propagation speed by 0.1%.

[137] The effect of overestimating the baseline lengths is to increase the apparent height of distant sources. Conversely, underestimating the baseline lengths would decrease the apparent heights. For sources below some altitude z_1 the measured time delay value $T_{4,2}$ will exceed the assumed transit time, making the hypotenuse shorter than the adjacent side in the right triangle of Figure 11d and $\cos\theta > 1$. Sources just above or at z_1 will appear to be on the network horizon, while sources below z_1 will be rejected, as if they have "disappeared" below the horizon. (Alternatively, if the $\cos\theta$ value is set to unity by the processing program, the sources will accumulate on the network horizon. This latter effect was noticed in initial processing of LMA observations

from Oklahoma in 1998.) For sources over or near the network the effect of small positional errors in the station locations is primarily to increase the chi-square values of the least squares solutions and does not significantly affect the source locations.

B4. Propagation Speed

[138] The propagation speed is a function of the dielectric constant of the Earth's atmosphere, which, in the VHF range, depends on altitude and water content. From *Doviak and Zrnić* [1993] the speed of radio waves is typically reduced from its free space value by 0.03% at sea level and by about 0.02% at 600 mbar pressure. Thus the propagation speed varies slightly with altitude, causing the signals to be refracted somewhat from their true location and arrival direction. Refraction has a significant effect only on distant storm observations, however, which are already substantially affected by the random measurement errors. Consequently, we have not attempted to include refraction effects in the present study; it usually suffices to use an average propagation speed.

[139] The LMA processing currently uses the 600 mbar speed, namely 0.02% less than the free space value $c \equiv 299{,}792{,}458\ \mathrm{m\ s^{-1}}$. In other words, the propagation speed is assumed to be $v = c/1.0002$. 600 mbar pressure corresponds to about 4.5 km altitude in the atmosphere, so the 600 mbar value would represent the average speed for sources at $\simeq$9 km altitude. The average speed would be slightly overestimated for sources at higher altitude and slightly underestimated for sources at lower altitude. At most, this incurs an error of <0.01%. The effect of a 0.01% propagation speed error would be to alter the distance r between a given station and the source by (0.01%)r or by 1 m for sources at 10 km range, 5 m at 50 km range, and 30 m at 300 km range. Such errors are small in comparison to the random timing errors.

[140] The above expresses the effect of propagation speed on the range to the source. The analysis can be made more specific by noting that, from equation (4), the range r of a distant source is inversely proportional to the propagation speed c. In finite difference form the differential expression for r is therefore

$$\frac{\Delta r}{r} = -\frac{\Delta c}{c}, \tag{B1}$$

where Δc is the error in c. Thus the fractional error in r is the negative of the fractional error in c. Overestimating c by 0.01% would underestimate r by the same fractional amount. At 100 km range the systematic error in r would be $\Delta r_c = -r(\Delta c/c) = -10$ m, as above. From equation (5) the random range error for a 70 km diameter network having 50 ns rms timing uncertainty is $\Delta r_t \simeq 350$ m rms. Therefore the systematic range error is 3% of the random error. At close ranges the speed error increases relative to the timing error but remains small in absolute terms (e.g., $\simeq$1 m at 10 km distance).

[141] The effect of a propagation speed error is magnified in directions transverse to r and for distant storms, can become comparable to the uncertainty due to timing errors. The magnification effect on height can be seen from the differential of $z = r\sin\theta$, where θ is the elevation angle to the source. For distant storms, θ is determined from equation (6), and the differential for z gives

$$\frac{\Delta z}{z} = -\cos^2\theta\left(\frac{r}{z}\right)^2\frac{\Delta c}{c} \simeq -\left(\frac{r}{z}\right)^2\frac{\Delta c}{c}. \tag{B2}$$

For sources at 10 km height and 100 km range the error in z is magnified by a factor of $(10)^2 = 100$ relative to the error for r. A 0.01% speed overestimate would therefore underestimate the apparent height of the source by 100 m. This result has been verified by processing data for the 25 June aircraft track with different values of the propagation speed. Such an error would still be less than that due to random timing errors, which is 300 m rms for a 70 km diameter network having 50 ns timing uncertainties.

[142] As seen for the other errors, it is the height of distant sources that is most affected by propagation speed errors rather than the range. Interestingly, use of the 600 mbar propagation speed guarantees a small systematic height error for distant storms. This is because the elevation angle depends on the time difference of arrival at the close and far stations along the direction of arrival, which for low elevation angle sources is determined by the propagation speed immediately above the Earth's surface. The 600 mbar value overestimates this speed by up to 0.01% and potentially by more if ground effects further slow the wave.

Appendix C: Range Uncertainties Outside the Network

C1. Simple Model Formulation

[143] The range of a source outside the network is determined from the curvature of the wavefront at stations transverse to the arrival direction, as indicated in Figure 11c. From the right triangle in Figure 11c, one has that

$$(D/2)^2 + r^2 = \left(r + cT_{13,0}\right)^2.$$

Simplifying and noting that $cT_{13,0} \ll D/2$ for sources at large ranges gives

$$r = \frac{D^2}{8cT_{13,0}} - \frac{cT_{13,0}}{2} \simeq \frac{D^2}{8cT_{13,0}}. \tag{C1}$$

The differential of this gives

$$dr = -\frac{D^2}{8cT_{13,0}^2}\,dT_{13,0} = -\frac{8r^2}{D^2}cdT_{13,0},$$

so that the rms uncertainty in r is

$$\Delta r = 8\left(\frac{r}{D}\right)^2 c\Delta T_{13,0}. \tag{C2}$$

The uncertainty in the range r is thus proportional to the arrival time uncertainty $\Delta T_{13,0}$ and increases as r^2, scaled by the network diameter D.

C2. Distant Storm Observations

[144] For distant storms, the experimentally observed variance of the lightning sources is the sum of the variances due to the storm size and to the measurement uncertainties. Denoting the standard deviation of the locations in the radial

and azimuthal directions as σ_{range} and σ_{azim}, respectively, the total variances are given by

$$\sigma^2_{radial} = \sigma^2_{\parallel storm} + \sigma^2_{range}$$

and

$$\sigma^2_{transverse} = \sigma^2_{\perp storm} + \sigma^2_{azim} ,$$

where $\sigma_{\parallel storm}$ and $\sigma_{\perp storm}$ are the standard deviations associated with the size of the storm itself in the radial and transverse directions, respectively. Assuming the storm extents are related by $\sigma_{\parallel storm} = f \cdot \sigma_{\perp storm}$, where f is a shape factor that can be greater or less than unity, the standard deviation of the range error is given by

$$\sigma^2_{range} = \sigma^2_{radial} - f^2\left[\sigma^2_{transverse} - \sigma^2_{azim}\right].$$

If f is not substantially different from unity, the effect of the azimuthal error σ_{azim} can be neglected in comparison to the range error σ_{range}, giving

$$\sigma^2_{range} \simeq \sigma^2_{radial} - f^2 \cdot \sigma^2_{transverse}. \quad (C3)$$

Finally, if the storms are circular or nearly circular, ($f \simeq 1$) so that

$$\sigma^2_{range} \simeq \sigma^2_{radial} - \sigma^2_{transverse}. \quad (C4)$$

Alternatively, if f is not close to unity, one can average the results over a number of storms in different directions from the network. Denoting the average by angle brackets, one has that $\langle f^{-2} \rangle \simeq 1$ if there is no systematic dependence of f on the direction of the storm or from storm to storm. Thus from equation (24),

$$\begin{aligned}\langle \sigma^2_{range} \rangle &= \langle \sigma^2_{radial} \rangle - \langle f^2 \cdot \sigma^2_{transverse} \rangle \\ &= \langle \sigma^2_{radial} \rangle - \langle f^2 \rangle \langle \cdot \sigma^2_{transverse} \rangle \\ &\simeq \langle \sigma^2_{radial} \rangle - \langle \sigma^2_{transverse} \rangle. \end{aligned} \quad (C5)$$

This result is the same as equation (C4) but applies to averages rather than individual storm values.

Appendix D: Pulse Transmitter and Data Encoder

[145] The pivotal component of the balloon-borne pulse transmitter is an integrated circuit oscillator in the frequency band (60–66 MHz) of the LMA. The oscillator (Fox, Incorporated KF090AT) has a control pin for turning on and off the 63 MHz oscillator with a digital logic level of 0 or 5 V. In our pulse transmitter the digital logic signal comes from one of the output pins of a microcontroller (Motorola 68HC12), which has special circuits for producing pulses with precise frequency and duration.

[146] The 63 MHz signal from the integrated circuit oscillator is amplified in two stages with GaAs power transistors (Motorola MRF136 and MRF171A). In order to reduce power consumption, the amplification of the power transistors is held at a low level by the microcontroller until just before the oscillator's 63 MHz pulse is gated out. The pulse duration was 125 ns (eight cycles of 63 MHz), which is the minimum width that could be produced by the microcontroller. The power emitted during the pulse was estimated to be about 60 W into a matched load. However, the source powers estimated by the LMA were only 1–2 W. The difference is presumed to be due to a mismatch between the transmitter and the wire antenna on the balloon package and to gain losses associated with the patterns of the transmitting and receiving antennas.

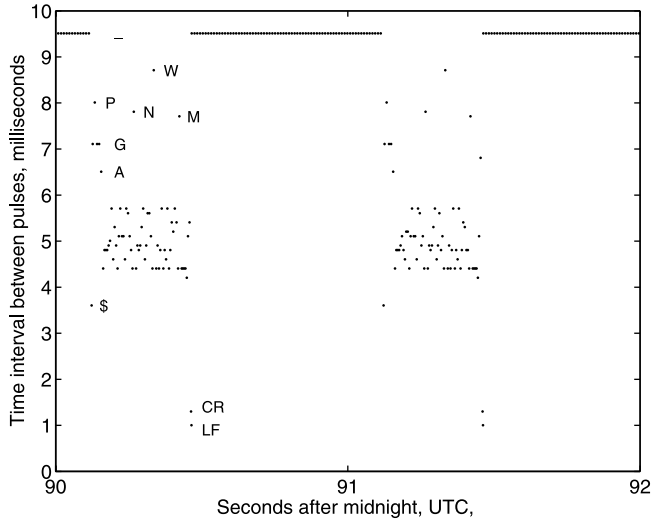

Figure D1. Time intervals between pulses as a function of time. Some of the corresponding characters are labeled. The character at 9.5 ms is an underscore, which filled intervals when the balloon-borne GPS receiver was not sending characters to the microcontroller. The cluster of characters between 4.2 and 5.7 ms are the numbers 0 to 9, commas, asterisks, and decimal points. The two strings shown in the figure are GPGGA,000129.51,3933.9830,N,10159.1883,W,1,09,0.9,06496, M,,,,*36 and GPGGA,000130.44,3933.9813,N,10159.1803, W,1,09,0.9,06500,M,,,,*3D. The first string gives the position of the balloon-borne receiver at 0001:29.51 UTC; the position was 39° 33.9830′N latitude, 101° 59.1883′W longitude and 6496 m above a reference surface. Nine satellites were being used by the GPS receiver.

[147] The microcontroller (1) searched for the appropriate serial string of position and time information from a global positioning system (GPS) receiver (Magellan GPS 310), (2) converted each character in the string to a time interval corresponding to the numerical equivalent of the character, and (3) gated the oscillator to produce pulses after each time interval.

[148] Each LMA receiver recorded the time each pulse was received with an uncertainty of about 40 ns. From the collection of times recorded at each receiver the position of the pulse transmitter and the time it emitted the pulse could be determined as if it were a pulse of radiation from lightning. In addition, by differencing the times of successive pulses, the numerical equivalent of each character in the string from the GPS receiver on the balloon could be recovered, thus providing a direct measure of the position of the balloon-borne instrument. Figure D1 shows the time interval between pulses from a single LMA station during a 2 s interval just after 0000 UTC. The time interval includes two strings from the GPS receiver. Some of the characters corresponding to the time intervals are shown in the figure, and the two character strings are given in the figure caption.

[149] In other applications the time intervals between pulses would not need to correspond to characters. Instead,

they could, for example, correspond to the numbers derived from a sensor or sensors attached to a computer via an analog-to-digital converter. In this case, the position of the instrument would be determined in only one way: by locating the sources of the pulses as the LMA does for lightning. The pulse transmitter/microcontroller combination allows the LMA to be used as a telemetry receiver that also gives the location of the transmitting instrument. Several identical instruments could be transmitting simultaneously, in which case the times to be subtracted to give time intervals would be selected to come from nearly the same locations; the instruments would be distinguished by their locations rather than by transmitting on separate frequencies.

[150] It is interesting to calculate the bit rate that can be transmitted by this unusual method of telemetry. The LMA itself establishes a minimum time interval between pulses because it records the time for only the largest amplitude pulse in successive time windows that are typically 80 or 100 μs in duration (but which can be reduced to 10 μs). In addition, if the Lightning Mapping Array is also being used to study lightning, most of the windows would probably be reserved to receive pulses from lightning. Thus the conversion from the value of a datum to a time interval between pulses could be a linear transformation such as

$$dt = dt_{\min} + dt_{\text{bit}}\, D, \tag{D1}$$

where $dt_{\min}$ is the minimum desired time interval between pulses, dt_{bit} is the time interval increment corresponding to an increase of 1 in a data word, and D is the data value. The time interval increment, dt_{bit}, must be greater than the uncertainty in the difference between the arrival times recorded by the LMA receivers, which is about 60 ns. If N is the word length, then the information content of each time interval between pulses is N bits, and the bit rate is

$$B = N/dt = N/(dt_{\min} + dt_{\text{bit}}\, D). \tag{D2}$$

Thus for this method of telemetry the bit rate depends on the data values. With a minimum interval between pulses of 1 ms and dt_{bit} = 120 ns the average bit rate is about 10^4 bits s^{-1}, with 10 bit words.

[151] In the situation in which the Lightning Mapping Array was used only as a telemetry receiver (in the absence of lightning) the bit rate could be increased by reducing the minimum duration between pulses.

[152] **Acknowledgments.** This work was supported by the U.S. National Science Foundation under grants ATM-9912073, ATM-0070934, and ATM-9601652. We thank David Proctor, Ken Cummins, and a third reviewer for their constructive comments and suggestions on the manuscript.

References

Behnke, S. A., R. J. Thomas, P. Krehbiel, and W. Rison (2003), Propagation speeds of lightning leaders throughout an entire flash using 10 μs time resolution 3D mapping data, *Eos Trans. AGU*, *84*(46), Fall Meet. Suppl., Abstract AE21A-1103.

Bevington, P. R. (1969), *Data Reduction and Error Analysis for the Physical Sciences*, McGraw-Hill, New York.

Boccippio, D. J., S. Heckman, and S. J. Goodman (2001), A diagnostic analysis of the Kennedy Space Center LDAR network: 1. Data characteristics, *J. Geophys. Res.*, *106*, 4769–4786.

Cummins, K. L., M. J. Murphy, E. A. Bardo, W. L. Hiscox, R. B. Pyle, and A. E. Pifer (1998), A combined TOA/MDF technology upgrade of the U.S. National Lightning Detection Network, *J. Geophys. Res.*, *103*, 9035–9044.

Darden, C., J. Burks, T. Bradshaw, D. Boccippio, S. Goodman, R. Blakeslee, E. McCaul, D. Buechler, J. Hall, and J. Bailey (2003), The integration of total lightning information into National Weather Service operations, *Eos Trans. AGU*, *84*(46), Fall Meet. Suppl., Abstract AE31B-03.

De Fatta, D. J., J. G. Lucas, and W. S. Hodgkiss (1988), *Digital Signal Processing: A System Design Approach*, 661 pp., John Wiley, Hoboken, N. J.

Demetriades, N. W. S., M. J. Murphy, and R. L. Holle (2004), The importance of total lightning in the future of weather nowcasting, paper presented at the Symposium on Planning, Nowcasting, and Forecasting in the Urban Zone, Am. Meteorol. Soc., Seattle, Wash., 11–15 Jan.

Doviak, R. J., and D. S. Zrnić (1993), *Doppler Radar and Weather Radar Observations*, 562 pp., Academic, San Diego, Calif.

Goodman, S. (2003), Atmospheric electrical activity and the prospects for improving short-term weather forecasting, paper presented at the 12th International Conference on Atmospheric Electricity, Int. Comm. on Atmos. Electr., Versailles, France, 9–13 June.

Gunn, R., W. C. Hall, and G. D. Kinzer (1946), Part I—The precipitation-static interference problem and methods for its investigation, *Proc. IRE*, *34*, 156–161.

Illingworth, A. J., and S. J. Marsh (1986), Static charging of aircraft by collisions with ice crystals, *Rev. Phys. Appl.*, *12*, 803–808.

Jones, J. J. (1990), Electric charge acquired by airplanes penetrating thunderstorms, *J. Geophys. Res.*, *95*, 16,589–16,600.

Koshak, W. J., and R. J. Solakiewicz (1996), On the retrieval of lightning radio sources from the time-of-arrival data, *J. Geophys. Res.*, *101*, 26,631–26,639.

Koshak, W. J., et al. (2004), North Alabama Lightning Mapping Array (LMA): VHF source retrieval algorithm and error analyses, *J. Atmos. Oceanic Technol.*, *21*, 543–558.

Krehbiel, P. R. (1981), An analysis of the electric field change produced by lightning, Ph.D. dissertation, Univ. of Manchester Inst. of Sci. and Technol., U. K.

Krehbiel, P. R., M. Brook, and R. A. McCrory (1979), An analysis of the charge structure of lightning discharges to ground, *J. Geophys. Res.*, *84*, 2432–2456.

Krehbiel, P. R., R. J. Thomas, W. Rison, T. Hamlin, J. Harlin, and M. Davis (2000), Lightning mapping observations in central Oklahoma, *Eos Trans. AGU*, *81*(3), 21–25.

Lang, T. J., et al. (2004), The Severe Thunderstorm Electrification and Precipitation Study (STEPS), *Bull. Am. Meteorol. Soc.*, in press.

Lennon, C. L. (1975), LDAR: New lightning detection and ranging system, *Eos Trans. AGU*, *56*(12), 991.

Lhermitte, R., and P. R. Krehbiel (1979), Doppler radar and radio observations of thunderstorms, *IEEE Trans. Geosci. Electron.*, *GE-17*, 162–171.

Maier, L., C. Lennon, T. Britt, and S. Schaefer (1995), LDAR system performance and analysis, paper presented at the 6th Conference on Aviation Weather Systems, Am. Meteorol. Soc., Boston, Mass.

Poehler, H. A. (1977), An accuracy analysis of the LDAR system, *NASA Contract. Rep., CR-154631*, 83 pp.

Proctor, D. E. (1971), A hyperbolic system for obtaining VHF radio pictures of lightning, *J. Geophys. Res.*, *76*, 1478–1489.

Proctor, D. E. (1981), VHF radio pictures of cloud flashes, *J. Geophys. Res.*, *86*, 4041–4071.

Proctor, D. E., R. Uytenbogaardt, and B. M. Meredith (1988), VHF radio pictures of lightning flashes to ground, *J. Geophys. Res.*, *93*, 12,683–12,727.

Rison, W., R. J. Thomas, P. R. Krehbiel, T. Hamlin, and J. Harlin (1999), A GPS-based three-dimensional lightning mapping system: Initial observations in central New Mexico, *Geophys. Res. Lett.*, *26*, 3573–3576.

Rison, W., P. Krehbiel, R. Thomas, T. Hamlin, and J. Harlin (2000), A time-of-arrival lightning mapping system with high time resolution, *Eos Trans. AGU*, *81*(48), Fall Meet. Suppl., Abstract A52C-01.

Shao, X. M., P. R. Krehbiel, R. J. Thomas, and W. Rison (1995), Radio interferometric observations of cloud-to-ground lightning phenomena in Florida, *J. Geophys. Res.*, *100*, 2749–2783.

Thomas, R. J., P. R. Krehbiel, W. Rison, T. Hamlin, J. Harlin, and D. Shown (2001), Observations of VHF source powers radiated by lightning, *Geophys. Res. Lett.*, *28*, 143–146.

T. Hamlin, J. Harlin, and P. R. Krehbiel, Physics Department, New Mexico Tech, Socorro, NM 87801, USA. (thamlin@nmt.edu; jharlin@nmt.edu; krehbiel@ibis.nmt.edu)

S. J. Hunyady and W. P. Winn, Langmuir Laboratory, Geophysical Research Center, New Mexico Tech, Socorro, NM 87801, USA. (hunyady@kestrel.nmt.edu; winn@loon.nmt.edu)

W. Rison and R. J. Thomas, Electrical Engineering Department, New Mexico Tech, Socorro, NM 87801, USA. (rison@ee.nmt.edu; thomas@nmt.edu)